CHALMERS
UNIVERSITY OF TECHNOLOGY

From Propane to Hydrogen and Plasma: CFD Modeling of the Transition Towards Fossil-Free High-Temperature Systems

Master's thesis in Innovative and Sustainable Chemical Engineering

ALEXANDER KINDBLOM

CHALMERS UNIVERSITY OF TECHNOLOGY
Gothenburg, Sweden 2026
www.chalmers.se

Master's thesis 2026

From Propane to Hydrogen and Plasma: CFD Modeling of the Transition Towards Fossil-Free High-Temperature Systems

ALEXANDER KINDBLOM

CHALMERS
UNIVERSITY OF TECHNOLOGY

Department of Environmental and Energy Sciences
Division of Energy Technology
High Temperature Process group
Chalmers University of Technology
Gothenburg, Sweden 2026

From Propane to Hydrogen and Plasma: CFD Modeling of the Transition Towards Fossil-Free High-Temperature Systems
ALEXANDER KINDBLOM

Supervisors: Saumitra Mishra, Adrian Gunnarsson, Thomas Allgurén & Henrik Ström, Department of Environmental and Energy Sciences & Department of Mechanical Engineering
Examiner: Klas Andersson, Department of Environmental and Energy Sciences

Master's Thesis 2026
Department of Environmental and Energy Sciences
Division of Energy Technology
High Temperature Process group
Chalmers University of Technology
SE-412 96 Gothenburg
Telephone +46 31 772 1000

Typeset in LaTeX
Printed by Chalmers Reproservice
Gothenburg, Sweden 2026

From Propane to Hydrogen and Plasma: CFD Modeling of the Transition Towards Fossil-Free High-Temperature Systems
ALEXANDER KINDBLOM
Department of Environmental and Energy Sciences
Chalmers University of Technology

Abstract

Energy-intensive industries such as iron ore and cement production rely on high-temperature heat traditionally supplied by fossil-fuel combustion. As these industries move towards lower-carbon alternatives, hydrogen combustion and carbon dioxide plasma heating are being considered as replacements, both of which change the conditions inside the heating unit. This thesis develops a computational fluid dynamics (CFD) model of the Chalmers 100 kW unit to characterize and compare the thermal and chemical behavior of propane combustion, hydrogen combustion, and CO_2 plasma heating.

A model of propane combustion was first developed in ANSYS Fluent and validated against experimental temperature and species measurements, comparing turbulence-chemistry models and reaction mechanisms. The validated framework was then adapted to the hydrogen and plasma cases, for which no experimental data are available.

The propane model reproduced the measured temperature and species fields once the flame had stabilized, though it predicted a lifted flame that did not anchor at the burner. The hydrogen flame anchored immediately and produced a hotter, more uniform outlet than propane. The plasma case, supplied with pre-heated dissociated CO_2, reached the highest and most radially uniform temperatures, with the dissociation products partially recombining as the gas cooled. At the same thermal load, the plasma configuration distributed heat more uniformly than hydrogen combustion.

The results indicate that CFD can provide a useful first characterization of these heating alternatives ahead of full-scale implementation, while highlighting the need for experimental validation of the hydrogen and plasma cases.

Keywords: CFD, combustion, propane, hydrogen, CO_2 plasma, high-temperature heating, decarbonisation, ANSYS Fluent

Acknowledgements

I would like to thank the Division of Energy Technology for the opportunity to do this thesis, and all the great people working in the division, who made it an enjoyable process with a welcoming atmosphere. I offer my sincere gratitude to my examiner, Klas Andersson, and my supervisors: Saumitra Mishra, Thomas Allgurén, Adrian Gunnarsson and Henrik Ström, who have given insightful advice, feedback and guidance. Their support and competence both inspired and motivated me.

Alexander Kindblom, Gothenburg, May 2026

List of Acronyms

Below is the list of acronyms that have been used throughout this thesis listed in alphabetical order:

CFD	Computational Fluid Dynamics
DNS	Direct Numerical Simulation
DOM	Discrete Ordinates Method
ED	Eddy Dissipation
EDC	Eddy Dissipation Concept
JL	Jones-Lindstedt
LES	Large Eddy Simulation
LHV	Lower Heating Value
ODE	Ordinary Differential Equation
RANS	Reynolds-Averaged Navier-Stokes
RSM	Reynolds Stress Model
RTE	Radiative Transfer Equation
SST	Shear-Stress Transport
URANS	Unsteady Reynolds-Averaged Navier-Stokes
WD	Westbrook-Dryer
WSGGM	Weighted Sum of Gray Gases Model

Nomenclature

Below is the nomenclature of Latin symbols, Greek symbols, and subscripts used throughout this thesis. Acronyms are listed separately.

Latin symbols

a_1	Stress limiter constant in SST k-ω model
$a_{\epsilon,k}$	Weight factor of gray gas k in WSGG model
A	Pre-exponential factor in Arrhenius expression
A_e, B_e	Empirical constants in Eddy Dissipation model
C_μ, $C_{\varepsilon 1}$, $C_{\varepsilon 2}$	Closure coefficients in k-ε model
$C_{j,n}$	Molar concentration of species j in reaction n
d	Inlet pipe diameter
D_h	Hydraulic diameter
Da	Damköhler number
E_a	Activation energy
F_2	Blending function in SST k-ω model
I_η	Spectral radiation intensity
$I_{\eta,b}$	Spectral blackbody radiation intensity
k	Turbulent kinetic energy per unit mass
$k_{f,n}$, $k_{b,n}$	Forward and backward rate constants for reaction n
L	Mean beam length
$\dot{m}$	Mass flow rate
$M_{w,i}$	Molecular weight of species i
M_θ, M_φ	Number of polar and azimuthal control angles per octant in DOM
p	Pressure; sum of partial pressures of emitting gases
r	Radial coordinate
$\vec{r}$	Position vector

R	Universal gas constant
R_i, R_o	Inner and outer radius of annular channel
R_c	Normalization radius for the swirl number
$R_{i,n}$	Net molar production rate of species i in reaction n
s	Path length
$\hat{s}$	Unit vector in direction of radiation propagation
S	Swirl number
t	Time
T	Temperature
u_i	Instantaneous velocity component in direction i
$\bar{u}_i$	Mean velocity component in direction i
u_i'	Fluctuating velocity component in direction i
u_τ	Friction velocity
$\bar{u}_z$, $\bar{u}_\theta$	Mean axial and tangential velocity components
x_i	Spatial coordinate in direction i
y	Distance from wall to first cell centre
y^+	Dimensionless wall distance
Y_i	Mass fraction of species i
Y_i^*	Fine-scale mass fraction of species i (EDC)

Greek symbols

β	Temperature exponent in Arrhenius expression
γ^*	Volume fraction of fine structures (EDC)
δ_{ij}	Kronecker delta
ε	Turbulent kinetic energy dissipation rate
ϵ	Emissivity
$\eta_{j,n}'$, $\eta_{j,n}''$	Forward and backward rate exponents
θ	Polar angle
κ	Model parameter related to fine-structure volume fraction (EDC)
κ_η	Spectral absorption coefficient
λ	Stoichiometric ratio (excess-air ratio)
μ	Dynamic viscosity
μ_t	Turbulent (eddy) dynamic viscosity

ν_T	Turbulent (eddy) kinematic viscosity
$\nu'_{i,n}$, $\nu''_{i,n}$	Stoichiometric coefficients of reactant and product species
ρ	Density
σ_k, σ_ε	Turbulent Prandtl–Schmidt numbers for k and ε
$\sigma_{s\eta}$	Spectral scattering coefficient
τ_w	Wall shear stress
τ^*	Fine-scale time scale (EDC)
ϕ	Generic instantaneous flow variable
$\bar{\phi}$, ϕ'	Mean and fluctuating components of ϕ
Φ_η	Scattering phase function
φ	Azimuthal angle
ω	Specific turbulent dissipation rate
Ω	Vorticity magnitude
Ω_i	Solid angle of incoming radiation direction

Subscripts

b	Blackbody value (radiation); backward (reaction)
f	Forward (reaction)
i, j	Tensor, coordinate or species indices; i also denotes inner radius and incoming direction
n	Reaction index
o	Outer (annular geometry)
P	Product species
$\mathcal{R}$	Reactant species
t, T	Turbulent
w	Wall
z	Axial direction
θ	Tangential direction
η	Spectral (wavenumber-dependent) quantity

Contents

List of Figures

List of Tables

1

Introduction

1.1 Background

Sweden has set a target to reach net-zero emissions of greenhouse gases by 2045 [1], requiring significant changes in energy-intensive industries. Two such Swedish industries, LKAB (iron ore) and Heidelberg Materials (cement), are investigating electrification as a route to reduce their reliance on fossil fuels. Heidelberg Materials is exploring direct electrification by replacing kiln burners with plasma torches, while LKAB is investigating indirect electrification through hydrogen as a fuel replacement. Both routes avoid the fossil CO_2 produced by conventional combustion: hydrogen combustion produces H_2O, and CO_2 plasma heating uses CO_2 as the working gas, heated by electrical energy rather than combustion.

Replacing the fuel or heat source changes the thermal and flow conditions inside the heating unit, and understanding these changes is relevant before the alternatives are implemented at full scale. Chalmers is in the process of modifying their existing 100 kW furnace to enable the study of how these alternatives operate. The flow in the unit is turbulent, and for the hydrogen case it is swirl-stabilized. Turbulent mixing governs where and how fast the fuel reacts, and therefore the shape of the flame and the heat release. Capturing this interaction between turbulence and chemistry is needed to predict the temperature and species fields, and is the main modeling challenge in this work.

Computational fluid dynamics (CFD) allows these configurations to be investigated, and is a particularly valuable tool for estimating field variables which are difficult to measure. Combining CFD models with experimental data therefore provides a more holistic understanding of the process. Additionally, CFD allows for prediction of alternative configurations and helps guide the design of future experimental studies.

1.2 Aim

The aim of this thesis is to develop and validate a CFD model of propane combustion in the Chalmers 100 kW unit, and subsequently adapt it to model hydrogen combustion and CO_2 plasma heating, in order to characterize and compare the thermal and chemical behavior of the three configurations. Specifically, centerline and radial profiles of temperature and major species composition are analyzed and compared

across the configurations.

1.3 Research Questions

- How well can the propane combustion model reproduce experimental data from the Chalmers 100 kW unit?

  This establishes a validated baseline that provides confidence in the selected models and settings, which are then carried over to the hydrogen and plasma cases. Validation is assessed by comparing simulated temperature and species profiles against available measurement data.

- What are the differences in temperature distribution and gas composition between propane, hydrogen and CO_2 plasma heating?

  Understanding these differences is relevant for assessing how the transition from fossil combustion to hydrogen or plasma heating affects the thermal field within the unit. The differences are quantified by comparing simulated centerline and radial temperature and species profiles across the three configurations.

1.4 Limitations

This work is limited to CFD modeling of the Chalmers 100 kW unit; no experimental work was conducted. Validation data is available only for the propane case. The hydrogen and plasma models represent a modified burner configuration under development, for which no experimental data exist, and rely on the validated propane model as a baseline with adaptations based on literature and available data. They are therefore presented as characterizations rather than validated predictions.

2

Theory

2.1 Turbulent Flow Modeling

Turbulent flows are characterized by fluctuating velocity fields that arise when viscous forces cannot dampen out fluctuations caused by inertial forces, a behavior commonly associated with high Reynolds numbers. They are chaotic in nature and contain swirling regions called eddies, which significantly enhance mixing compared to laminar flow. These aspects make turbulence an important flow feature in combustion processes where fuel-air mixing governs the availability for the reactions to occur. Turbulence is also dissipative in nature, where energy is extracted from the mean flow by large eddies and transferring to progressively smaller isotropic scales, ultimately being dissipated as heat through viscous effects [2].

Resolving all scales of turbulent motion directly as done in Direct Numerical Simulation (DNS) requires immense computational resources that exceed what is currently possible for engineering applications. As such, some form of turbulent modeling needs to be applied. The Reynolds decomposition is used to describe a flow's instantaneous variables by their mean part $\bar{\phi}$ and fluctuating part ϕ'.

$$\phi = \bar{\phi} + \phi' \tag{2.1}$$

Applying this decomposition to the Navier-Stokes equations and time-averaging yields the Reynolds-Averaged Navier-Stokes (RANS) equations. The time-averaged momentum equation is presented as it introduces an additional term, the Reynolds stress tensor $-\rho\overline{u_i' u_j'}$, representing the transfer of momentum by turbulent fluctuations.

$$\rho\frac{\partial \bar{u}_i}{\partial t} + \rho\bar{u}_j\frac{\partial \bar{u}_i}{\partial x_j} = -\frac{\partial \bar{p}}{\partial x_i} + \frac{\partial}{\partial x_j}\left(\mu\frac{\partial \bar{u}_i}{\partial x_j} - \rho\overline{u_i' u_j'}\right) \tag{2.2}$$

This term contains products of fluctuating velocity components, introducing six additional unknowns and resulting in an unclosed system known as the closure problem. The following sections present turbulence models that provide closure, either through the Boussinesq hypothesis which models the Reynolds stresses with a lumped turbulence viscosity, or by solving transport equations directly for each stress component.

2.1.1 The $k-\varepsilon$ Model

The Boussinesq hypothesis assumes that the momentum transport from turbulence is a diffusive, isotropic process, and as such the Reynolds stresses can be modeled with a single scalar called turbulent viscosity μ_T (eddy viscosity) [2].

$$-\rho\overline{u_i' u' j} = \mu_t\left(\frac{\partial \bar{u}_i}{\partial x_j} + \frac{\partial \bar{u}_j}{\partial x_i}\right) - \frac{2}{3}\rho k \delta ij \tag{2.3}$$

In equation 2.3 k is the turbulent kinetic energy per unit mass and is defined as half the trace of the Reynolds stress tensor $k = (1/2)\overline{u_i' u'}_i$. δ_{ij} is the Kronecker delta, which is equal to one if $i = j$ and zero otherwise [2]. The turbulent viscosity is modeled as:

$$\mu_t = \rho C_\mu \frac{k^2}{\varepsilon} \tag{2.4}$$

To determine μ_T, transport equations are solved for both k and the energy-dissipation rate ε. Physically, ε represents the rate at which turbulent kinetic energy is dissipated into heat through viscous effects [2].

$$\frac{\partial(\rho k)}{\partial t} + \frac{\partial(\rho \bar{u}_j k)}{\partial x_j} = \mu_t\left[\left(\frac{\partial \bar{u}_i}{\partial x_j} + \frac{\partial \bar{u}_j}{\partial x_i}\right)\frac{\partial \bar{u}_i}{\partial x_j}\right] - \rho\varepsilon + \frac{\partial}{\partial x_j}\left[\left(\mu + \frac{\mu_t}{\sigma_k}\right)\frac{\partial k}{\partial x_j}\right] \tag{2.5}$$

$$\frac{\partial(\rho \varepsilon)}{\partial t} + \frac{\partial(\rho \bar{u}_j \varepsilon)}{\partial x_j} = C_{\varepsilon 1}\frac{\varepsilon}{k}\mu_t\left[\left(\frac{\partial \bar{u}_i}{\partial x_j} + \frac{\partial \bar{u}_j}{\partial x_i}\right)\frac{\partial \bar{u}_i}{\partial x_j}\right] - C_{\varepsilon 2}\rho\frac{\varepsilon^2}{k} + \frac{\partial}{\partial x_j}\left[\left(\mu + \frac{\mu_t}{\sigma_\varepsilon}\right)\frac{\partial \varepsilon}{\partial x_j}\right] \tag{2.6}$$

The modeling constants: C_μ, $C_{\varepsilon 1}$, $C_{\varepsilon 2}$, σ_k, σ_ε are the five closure coefficients in the $k-\varepsilon$ model and are empirically determined to apply for a large range of turbulent flows. Specifically, σ_k and σ_ε are the turbulent Prandtl-Schmidt numbers for k and ε respectively [2].

The standard $k-\varepsilon$ model is widely used, however it has subpar accuracy in flows involving streamline curvature, swirling flows and axisymmetric jets. These inaccuracies stem from the Boussinesq hypothesis assumption of isotropy and the way in which dissipation is modeled. This is because the model was calibrated for high-Reynolds-number flows that are near isotropy, where local equilibrium between generation of k and dissipation ε holds [2]. As such, modifications of the standard $k-\varepsilon$ model have been proposed in order to address these weaknesses by tuning the model parameters. One such modification is the realizable $k-\varepsilon$ model, which introduces a realizable constraint on the predicted stress tensor. In the standard model, the normal stress can become negative in flows with large mean strain rates. The realizable variant instead uses a variable C_μ that ensures that the normal stresses are positive under all flow conditions and thus is expected to perform better in flows involving rotation and separation [2]. Additionally, the ε equation is modified based on the dynamic equation of the mean-square vorticity fluctuation [3].

Since the $k-\varepsilon$ model was derived for high-Reynolds-number flows, it breaks down in the near-wall region where viscous effects dominate over turbulent effects, causing the model to incorrectly predict k and ε in this near-wall region. There are two ways of handling this, either by modifying the model in the viscosity-affected region and using a sufficiently fine mesh, which is computationally expensive, or by applying wall functions. The wall function approach uses semi-empirically derived rules based on the law of the wall to estimate velocities $\bar{u}_i$, k and ε in the first cell close to the wall [2].

The near-wall region is commonly expressed as a dimensionless wall distance y^+, defined as:

$$y^+ = \frac{\rho u_\tau y}{\mu} \tag{2.7}$$

where $u_\tau = \sqrt{\tau_w/\rho}$ is the friction velocity, τ_w is the wall shear stress and y is the distance from the wall to the first cell center. The near-wall region is classified into three regions [2]:

i. Viscous sub-layer $0 < y^+ < 5$

ii. Buffer sub-layer $5 < y^+ < 30$

iii. Fully turbulent sub-layer $30 < y^+ < 400$

Wall functions are applied in the buffer and viscous sub-layers, bridging these regions semi-empirically so that the first cell center falls within the fully turbulent sub-layer where the $k-\varepsilon$ model is valid. The standard wall functions are based on assumptions of constant shear and local equilibrium between production and dissipation. In flows where these assumptions do not apply, such as when adverse pressure gradients are present and flow separation and reattachment may occur, the standard wall functions are not able to capture these phenomena accurately and thus require modifications. These modifications lead to different types, such as non-equilibrium wall functions, that relax equilibrium conditions and include a log law for the mean velocity which is sensitive to the pressure-gradient effects [2].

2.1.2 The $k-\omega$ Model

The $k-\omega$ model is another two-equation model based on the Boussinesq hypothesis, similar to $k-\varepsilon$. Instead of using energy dissipation ε, the specific dissipation $\omega \propto \varepsilon/k$ is used and represents the inverse of the time scale on which dissipation occurs [2]. The turbulent viscosity for the ω based model is calculated from:

$$\mu_T = \frac{\rho k}{\omega} \tag{2.8}$$

An advantage of the $k-\omega$ model is that it can be integrated directly to the wall without wall functions, accurately resolving the viscous sub-layer provided the mesh is sufficiently fine ($y^+ < 5$). A widely used variant of the $k-\omega$ model is the Shear-Stress Transport (SST) formulation that combines the near-wall accuracy of $k-\omega$

with the freestream robustness of $k - \varepsilon$. In the SST variant, μ_T is modified with a stress limiter to improve prediction of adverse pressure gradient flows:

$$\mu_T = \frac{\rho a_1 k}{\max(a_1 \omega; \Omega F_2)} \tag{2.9}$$

Where a_1 is a model constant, Ω is the absolute value of vorticity and F_2 is a blending function equal to unity in the near-wall region and zero in the freestream [4].

2.1.3 The Reynolds Stress Model

The Reynolds Stress Model (RSM) does not use the Boussinesq hypothesis and as such avoids the assumption of isotropy. Instead RSM closes the RANS equations by solving additional non-linear transport equations for each Reynolds stress. The transport equation for each Reynolds stress component contain a pressure-strain correlation term, which redistributes turbulent kinetic energy among the stress components and allows the model to capture stress anisotropy. This makes RSM particularly well suited for flows involving streamline curvature, strong swirl and rotation, where anisotropic stress effects are significant. The drawback is that six additional partial differential equations for the stresses and one for the energy-dissipation rate ε need to be solved, hence the model is much more computationally expensive [2].

2.2 Swirling Flames

Swirl is the rotation of the flow around the central axis of the burner nozzle. A common way to introduce swirl is by including angled fins in the airflow passage, imparting angular momentum to the axial flow. This allows control of the flame by inducing different amounts of swirl, where higher swirl tends to enhance mixing, widening the flame radially while shortening it axially compared to a non-swirling jet. Using a high enough swirl, an internal recirculation zone forms within the flame and recirculates hot combustion products back towards the burner nozzle [5], providing a continuous ignition source and stabilizing the flame.

The degree of swirl is commonly quantified by the dimensionless swirl number S, defined following the general framework of Gupta et al. [6], adapted for annular geometry by integrating over the annular limits R_i to R_o and neglecting pressure and turbulent stress contributions:

$$S = \frac{\int_{R_i}^{R_o} \rho \bar{u}_z \bar{u}_\theta r^2 dr}{R_c \int_{R_i}^{R_o} \rho \bar{u}_z^2 r dr} \tag{2.10}$$

Where $\bar{u}_z$ and $\bar{u}_\theta$ are the axial and tangential velocity components respectively, r is the radius and R_c is the normalization radius set to R_o of the annular channel.

2.3 Turbulent-Chemistry Interaction

Turbulent reactive flows involve complex interactions between turbulent mixing and chemical reactions, these operate at different time and length scales. The ratio of these scales is characterized by the Damköhler number, which determines whether reactions are mixing-limited or kinetics-limited [2].

$$Da = \frac{\text{Typical time required for mixing}}{\text{Typical time required for chemical reactions}} \tag{2.11}$$

A high Damköhler number indicates that mixing is slow relative to chemistry, meaning reactions are mixing-limited. A low Damköhler number indicates that chemistry is slow relative to mixing, meaning reactions are kinetics-limited. Accurately capturing this interaction is challenging, and several models have been developed with different assumptions and levels of complexity. An overview of some of the most common models is presented below.

2.3.1 Finite Rate

The Finite Rate model calculates reaction rates using the Arrhenius expression without accounting for the effects of turbulent fluctuations on the reaction rate [7]. This makes the model suitable for laminar flames but inaccurate in turbulent flows where concentration fluctuations significantly affect reaction rates. The reaction rate constant k_r is calculated from the Arrhenius expression:

$$k_r = AT^{\beta} e^{-\frac{E_a}{RT}} \tag{2.12}$$

where A is the pre-exponential factor, β is the temperature exponent, E_a is the activation energy and R is the universal gas constant. The net molar production rate of species i in reaction n is then given by [7]:

$$R_{i,n} = \left(\nu''_{i,n} - \nu'_{i,n}\right)\left(k_{f,n} \prod_{j=1}^{N} [C_{j,n}]^{\eta'_{j,n}} - k_{b,n} \prod_{j=1}^{N} [C_{j,n}]^{\eta''_{j,n}}\right) \tag{2.13}$$

where $k_{f,n}$ is the forward rate constant for reaction n computed from Equation 2.12, $k_{b,n}$ is the backward rate constant, $\nu'_{i,n}$ and $\nu''_{i,n}$ are the stoichiometric coefficients for reactant and product species respectively, $C_{j,n}$ is the molar concentration of species j, and $\eta'_{j,n}$ and $\eta''_{j,n}$ are the forward and backward rate exponents.

2.3.2 Eddy Dissipation

The Eddy Dissipation (ED) model is based on the assumption that in many turbulent flames, chemical reactions are fast relative to turbulent mixing. In such cases the overall reaction rate is controlled by the rate at which turbulence mixes reactants at the molecular level rather than by chemical kinetics. This allows for combustion

to be modeled by neglecting complex chemical kinetic rates and reactants are instead assumed to burn upon mixing [7]. The model, based on work by Magnussen and Hjertager [8], relates the reaction rate to the inverse time constant of turbulence ε/k, representing the rate of dissipation of turbulent eddies, which determines the rate of molecular mixing of reactants [8]. The net rate of production of species i due to reaction n is given by the smaller of the two expressions [7]:

$$R_{i,n} = (\nu''_{i,n} - \nu'_{i,n}) M_{w,i} A_e \rho \frac{\varepsilon}{k} \min_{\mathcal{R}} \left(\frac{Y_{\mathcal{R}}}{\nu'_{\mathcal{R},n} M_{w,\mathcal{R}}} \right) \tag{2.14}$$

$$R_{i,n} = (\nu''_{i,n} - \nu'_{i,n}) M_{w,i} A_e B_e \rho \frac{\varepsilon}{k} \frac{\sum_P Y_P}{\sum_j^N \nu''_{j,n} M_{w,j}} \tag{2.15}$$

where $Y_{\mathcal{R}}$ is the mass fraction of a reactant species $\mathcal{R}$, Y_P is the mass fraction of a product species P, $M_{w,i}$ is the molecular weight of species i and $A_e = 4.0$ and $B_e = 0.5$ are empirical constants [7]. Equation 2.14 limits the reaction based on the availability of reactants, equation 2.15 limits the reaction based on the availability of combustion products, which must be present for the reaction to proceed. The actual reaction rate is the minimum of the two, thus the model ensures that the locally limited quantity controls the combustion.

Since the model does not require Arrhenius parameters, it is computationally efficient. However, since combustion proceeds where there is turbulence and products present, combustion can proceed at unrealistic locations. This is often acceptable for non-premixed flames, but in premixed configurations it may cause the reactants to ignite upstream of the flame stabilizer. Additionally, the model is only accurate for one- or two-step global reaction mechanisms. This is because multi-step mechanisms rely on Arrhenius rates that differ between reactions, whereas the ED model assigns the same turbulent rate to all reactions [7].

2.3.3 Finite Rate/Eddy Dissipation

The Finite Rate/Eddy Dissipation model combines the two aforementioned models. In this model both the Arrhenius rates and eddy-dissipation rates are calculated, the net reaction rate is then taken as the minimum of these two rates [7]. In practice, the finite-rate kinetics acts as a switch, preventing reactions upstream of the flame stabilizer. Once the flame is ignited, the eddy dissipation rate is generally smaller than the Arrhenius rate and the reaction rate becomes mixing limited [7].

2.3.4 Eddy Dissipation Concept

The Eddy Dissipation Concept (EDC) is an extension of the ED model that allows for detailed chemical mechanisms to be incorporated in turbulent flows [9]. The model is based on the concept that the fine structures responsible for the main part of turbulent dissipation are generated in highly strained regions between larger eddies as thin vortex sheets or tubes of vorticity [9]. Within these fine structures,

reactants can be assumed to be mixed at the molecular scale, and it is here that chemical reactions are assumed to occur [9].

In the EDC model, these fine structures occupy a fraction of the computational cell characterized by a volume fraction γ^*. Combustion within the fine structures is modeled as a constant pressure reactor, where reactions proceed over a time scale τ^* and are integrated numerically using an ODE solver [7]. The source term for mean species i is modeled as [7]:

$$R_i = \rho\kappa\frac{Y_i^* - Y_i}{\tau^*} \tag{2.16}$$

where Y_i^* is the fine-scale species mass fraction after reacting over the integration time scale τ^*, and κ is a model parameter related to the volume fraction of fine structures. The volume fraction γ^* and time scale τ^* are both derived from k and ε [7][9]. Since detailed Arrhenius kinetics are solved within the fine structures, the model is able to include kinetically controlled species and slow chemistry effects, unlike the ED model. However, the numerical integration of detailed mechanisms is computationally expensive [7].

2.3.5 Reaction Mechanisms

Combustion of hydrocarbons consists of several hundred elementary and radical reactions [5]. Including all of these would be prohibitively expensive in CFD simulations. Instead, global reaction mechanisms address these constraints by representing combustion through a small number of overall reactions [5]. Two global mechanisms for propane combustion are considered in this work: the two-step Westbrook-Dryer mechanism, provided as a material mixture in Fluent 2025R2, and the four-step Jones-Lindstedt mechanism [10]. The reactions and corresponding rate parameters are presented in Tables 2.1 and 2.2. The Westbrook-Dryer rate parameters are the Fluent default values and are not reproduced here.

Table 2.1: Two-step Westbrook-Dryer and four-step Jones-Lindstedt global reaction mechanisms for propane combustion.

	Reaction	
Westbrook-Dryer (2-step)		
R1	$C_3H_8 + 3.5\,O_2 \longrightarrow 3\,CO + 4\,H_2O$	irreversible
R2	$CO + 0.5\,O_2 \rightleftharpoons CO_2$	reversible
Jones-Lindstedt (4-step)		
R1	$C_3H_8 + 1.5\,O_2 \longrightarrow 3\,CO + 4\,H_2$	irreversible
R2	$C_3H_8 + 3\,H_2O \longrightarrow 3\,CO + 7\,H_2$	irreversible
R3	$H_2 + 0.5\,O_2 \rightleftharpoons H_2O$	reversible
R4	$CO + H_2O \rightleftharpoons CO_2 + H_2$	reversible

Table 2.2: Arrhenius rate constants for the Jones-Lindstedt mechanism [10], $k = AT^{\beta}\exp(-E_a/RT)$. The Westbrook-Dryer rate parameters are the Fluent default values and are not reproduced here.

	Reaction order	A	β	E_a
R1	$[C_3H_8]^{0.5}\,[O_2]^{1.25}$	4×10^{11}	0	30.0
R2	$[C_3H_8]\,[H_2O]$	3×10^{8}	0	30.0
R3	$[H_2]^{0.25}\,[O_2]^{1.5}$	8.5×10^{15}	-1	40.0
R4	$[CO]\,[H_2O]$	2.75×10^{9}	0	20.0

Units consistent with kmol, m, s; E_a in kcal/mol.

Global reaction mechanisms ensure that heat from combustion is not released at one localized position, providing a more physically realistic representation of the flame. For systems with a few species, simpler schemes can be used without losing too much detail; hydrogen combustion is such a system and can be written in terms of its elementary reactions [5].

2.4 Radiation Model

In combustion, especially in the flame region, radiation is the dominating heat transfer mechanism since it scales with temperature to the fourth power. In combustion, radiation interacts with the absorbing, emitting and scattering medium, hence these are important aspects to consider when radiation is the dominating mechanism [11]. When considering a small cylindrical volume element, the radiative intensity at steady state can be described by the Radiative Transfer Equation (RTE) [11]:

$$\frac{\partial I_\eta}{\partial s} = \kappa_\eta I_{\eta,b} - (\kappa_\eta + \sigma_{s\eta})I_\eta + \frac{\sigma_{s\eta}}{4\pi}\int_{4\pi} I_\eta(\hat{s}_i)\Phi_\eta(\hat{s}_i, \hat{s})d\Omega_i \tag{2.17}$$

where i, η and b subscripts denote incoming, wavenumber and blackbody value respectively, and,

I_η = spectral radiation intensity	s = path length
$\hat{s}$ = unit vector in direction of propagation	κ_η = absorption coefficient
$\hat{s}_i$ = unit vector of incoming direction	$\sigma_{s\eta}$ = scattering coefficient
Φ_η = scattering phase function	Ω_i = solid angle

In equation 2.17, the term on the left-hand side is the intensity gradient in the s direction. The first term on the right-hand side represents the increase in intensity due to emission of radiation from the volume element. The second term on the right side is the reduction of intensity due to absorption and scattering in other direction than propagation by the volume element. The final term represents the increase in intensity due to scattering from all other directions into the direction of propagation $\hat{s}$ [12].

In gaseous combustion, scattering is negligible as no large particles are present [12], hence equation 2.17 can be simplified to the form:

$$\frac{\partial I_\eta}{\partial s} = \kappa_\eta (I_{\eta,b} - I_\eta) \tag{2.18}$$

2.4.1 Discrete Ordinates Method

The Discrete Ordinates Method (DOM) is a way to discretize the RTE into a finite number of partial differential equations. This is done by solving for a subset of discrete directions $\hat{s}$ spanning the total solid angle range of 4π [11]. The angular coordinate system is illustrated in Figure 2.1, where θ and φ are the polar and azimuthal angles respectively.

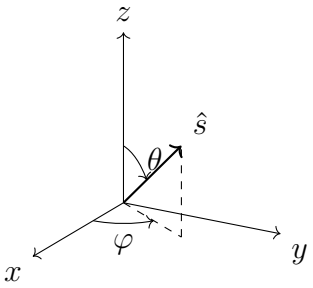

Figure 2.1: Angular coordinate system for the discrete ordinates method.

The total solid angle is discretized into $M_\theta \times M_\varphi$ control angles in each octant [7]. Neglecting scattering, as justified in Section 2.4, the DOM solves the simplified RTE for each discrete direction $\hat{s}$ [11].

$$\hat{s}_m \cdot \nabla I_\eta(\vec{r}, \hat{s}_m) + \kappa_\eta I_\eta(\vec{r}, \hat{s}_m) = \kappa_\eta I_{\eta,b} \tag{2.19}$$

where $\vec{r}$ is the position vector. In three-dimensional geometries, a total of $8M_\theta M_\varphi$ transport equations are solved, one for each discrete direction. The accuracy of the solution depends on the resolution of the angular discretization, with computational cost scaling $\propto M_\theta M_\varphi$, thus care should be taken when implementing discretization for DOM in practice.

2.4.2 Weighted Sum of Gray Gases

Combustion gases such as CO_2 and H_2O are non-gray, meaning they absorb and emit radiation only in specific spectral bands rather than uniformly across all wavelengths. Accurately resolving this spectral dependence is computationally expensive, and the Weighted Sum of Gray Gases (WSGG) model provides a practical approximation by replacing the non-gray gas with a weighted sum of gray gases and one clear gas [11]. In other words, the heat transfer contribution of each gray gas is calculated independently and then summed after multiplying with weight factors to provide the total heat flux [11]. The emissivity of the gas is calculated as:

$$\epsilon = \sum_{k=0}^{K} a_{\epsilon,k}(1 - e^{-\kappa_k pL}) \tag{2.20}$$

where $a_{\epsilon,k}$ is the weight factor of the fictitious gas k, κ_k is the absorption coefficient of corresponding gas, p is the sum of partial pressures of all emitting gases and the mean beam length is denoted L [11]. The weight factors are usually determined by temperature dependent correlations, the absorption coefficient for the clear gas is zero and accounts for spectral regions of the transparent gas [12].

3

Methods

This chapter describes the computational setup used to simulate three combustion configurations in the Chalmers 100 kW unit: propane combustion, hydrogen combustion, and plasma heating. The propane case serves as a validation baseline against available experimental data. The validated modeling approach is then adapted to simulate hydrogen combustion and plasma heating, for which no direct experimental reference data are available. Sections 3.1–3.5 describe shared aspects of the setup: experimental reference data, operating conditions, burner geometry, the air distribution study and lance study used to determine inlet boundary conditions. Sections 3.6–3.8 then detail the case-specific configurations.

3.1 Experimental Reference Data for Propane Validation

The experimental reference data used for validation was obtained from measurements conducted on the Chalmers 100 kW unit. No equivalent validation data is available for the hydrogen or plasma cases at this time. Measurements were performed with 100% propane at a mass flow rate of 1.73 $\mathrm{g\,s^{-1}}$ and a stoichiometric ratio $\lambda = 1.15$. The flue gas composition, summarized in Table 3.1, is reported assuming complete combustion.

Table 3.1: Flue gas composition assuming complete combustion of propane at $\dot{m} = 1.73\ \mathrm{g\,s^{-1}}$ and $\lambda = 1.15$.

O_2 [%wet]	O_2 [%dry]	CO_2 [%wet]	CO_2 [%dry]	H_2O [%]
2.55	2.95	10.21	11.82	13.61

The measurement campaign was conducted on the same burner described in Section 3.3, with one notable difference, the experimental configuration included cooling rods which are not included in any of the simulations. The heat extraction by the cooling rods is partially accounted for by prescribing measured wall temperatures, as described in Section 3.6.

Measurements were extracted at ports M2-M5 of temperature and composition of O_2, CO, CO_2, H_2O and NO. For each port, measurements were taken at dis-

crete radial positions from the centerline outward to the wall. Figure 3.1 shows the schematic overview of the furnace and Table 3.2 summarizes the vertical positioning of the ports. Measurements at ports M1 and M7 were not available.

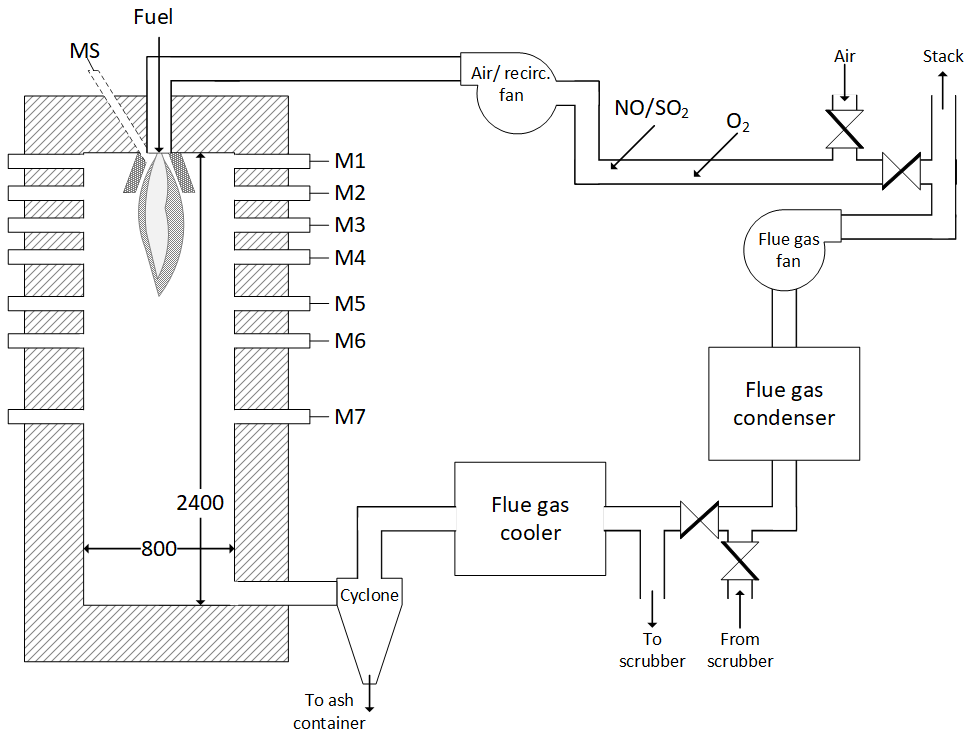

Figure 3.1: Schematic overview of the furnace.

Table 3.2: Vertical placements of the measuring ports in the furnace.

Port	M1	M2	M3	M4	M5	M6	M7
Distance [mm]	46	215	385	554	801	999	1401

The data from M2-M5 are from the same measurement campaign. Data from M6 is available for species composition only and is from a separate campaign. It is included in the results when presenting species data as an indicative reference. The full set of the measurement data is provided in Appendix A.1.

3.2 Operating Conditions and Stoichiometry

The mass flow rate of propane ($1.73\,\mathrm{g\,s^{-1}}$) corresponds to a thermal input of approximately 80 kW based on the lower heating value of propane, LHV = $46.1\,\mathrm{MJ\,kg^{-1}}$ [13]. The complete combustion reaction for propane is:

$$C_3H_8 + 5\,O_2 \longrightarrow 3\,CO_2 + 4\,H_2O \tag{3.1}$$

The total air mass flow rate required at $\lambda = 1.15$ is calculated as:

$$\dot{m}_{\text{air}} = \lambda \cdot \frac{5}{0.21} \cdot \frac{M_{\text{air}}}{M_{\text{propane}}} \cdot \dot{m}_{\text{propane}} = 31.1 \text{ g s}^{-1} \tag{3.2}$$

where $M_{\text{air}} = 28.96 \text{g mol}^{-1}$ and $M_{\text{fuel}} = 44.10 \text{g mol}^{-1}$. Both fuel and air enter the burner at room temperature, taken as $T_{\text{inlet}} = 298$ K in the simulations. The furnace operates at a slight overpressure in practice, since the deviation is small, the effect on gas density and flow properties is negligible. Operating pressure is therefore assumed to be atmospheric in all simulations.

The thermal input of the hydrogen case is 40 kW to allow for comparison with the plasma case, the mass flow rate of hydrogen was then similarly determined based on the lower heating value of 120.087 MJ kg^{-1} [13] resulting in 0.33 g s^{-1}. The complete combustion reaction for hydrogen is:

$$\text{H}_2 + \frac{1}{2}\,\text{O}_2 \longrightarrow \text{H}_2\text{O} \tag{3.3}$$

The total air mass flow rate for the hydrogen case is then calculated as:

$$\dot{m}_{\text{air}} = \lambda \cdot \frac{0.5}{0.21} \cdot \frac{M_{\text{air}}}{M_{\text{hydrogen}}} \cdot \dot{m}_{\text{hydrogen}} = 13.10 \text{ g s}^{-1} \tag{3.4}$$

The plasma case operates with pure CO_2 at a load of 40 kW and a volumetric flow rate of 150 SLPM. The corresponding mass flow rate of CO_2 is 4.91 g s^{-1}, with no oxidizer fed to the system. The reaction of interest is the dissociation of CO_2, which for completion is presented:

$$\text{CO}_2 \longleftrightarrow \text{CO} + \text{O} \tag{3.5}$$

3.3 Burner Geometry

The burner geometry consists of a cylindrical lance assembly mounted at the top of the furnace, delivering fuel and air into the combustion chamber through a set of concentric channels. The same hardware is used for both the propane and hydrogen cases; the channels active in each case differ depending on the fuel, as described in Sections 3.6 and 3.7. The plasma case uses a different configuration in which the lance is replaced and is described separately in Section 3.8.

A schematic of the radial placements of the channels is presented in Figure 3.2. Radially outward from the centerline, the lance contains: a central channel for hydrogen injection, a surrounding propane channel ending with eight perimeter holes and a 1 mm annular gap at the swirler exit, a primary air channel with swirl fins angled at 45°, and a secondary air channel with fins angled at 15°. The channel dimensions are summarized in Table 3.3.

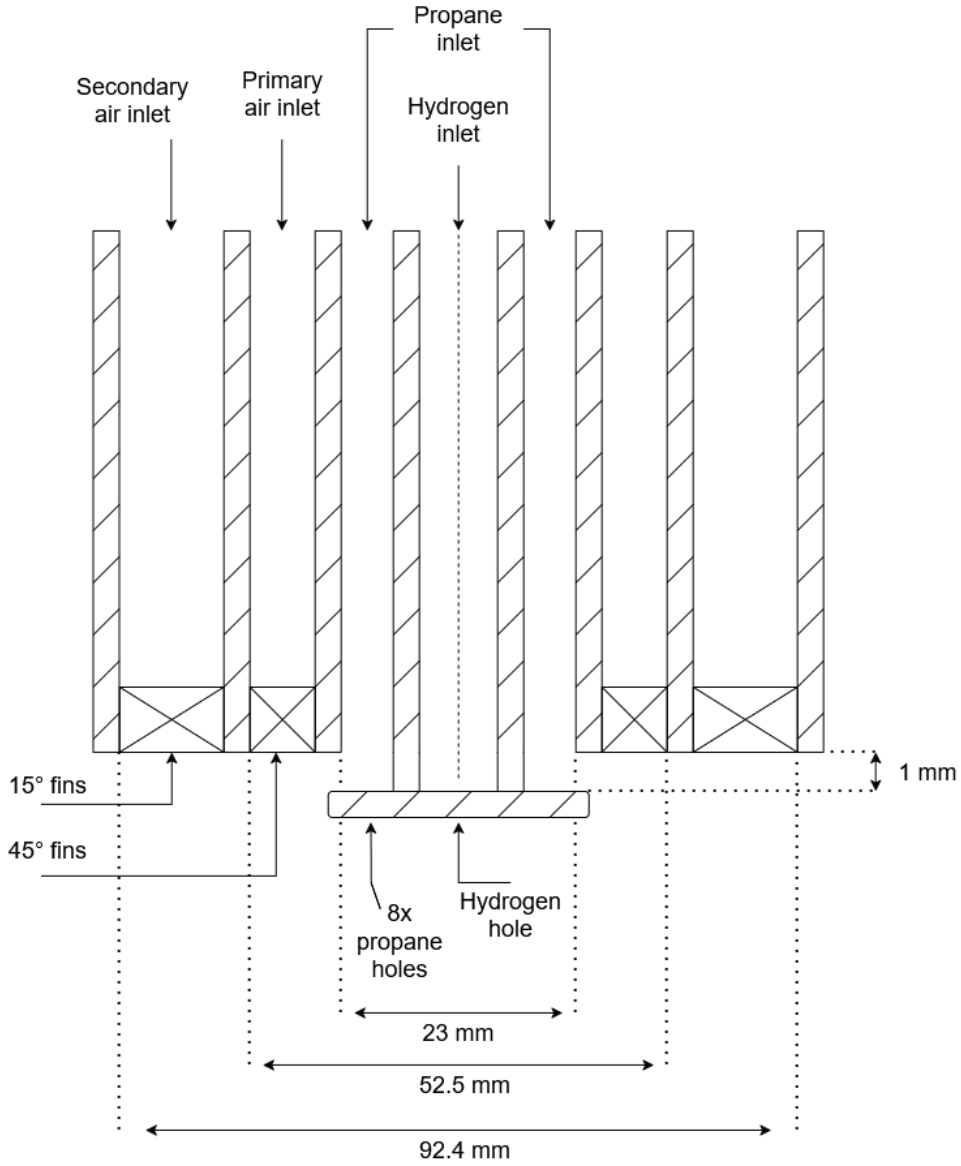

Figure 3.2: A schematic of the burner geometry in Chalmers 100 kW furnace.

Table 3.3: Lance dimensions for Chalmers 100 kW furnace.

Part	Inner diameter [mm]	Outer diameter [mm]	Notes
Hydrogen channel		12	
Hydrogen injection		4	
Propane channel	17	23	
Propane injection		2	8 holes (+1mm gap)
Primary channel	33.7	52.5	45° fins ($S = 0.79$)
Secondary channel	60.3	92.4	15° fins ($S = 0.21$)

The air register is fitted with angled fins to induce swirl to the primary and secondary air streams. The manufacturing drawings specify fin angles presented in Table 3.3

with their corresponding swirl numbers S. On-site measurements of the hardware indicate fin angles broadly consistent with the design values, with some deviation noted on the fins; precise measurement was complicated by the handmade construction. The drawings are taken as the design reference for the simulations.

3.4 Air Distribution Study

The air that feeds to the furnace consists of a main channel, where the air is driven by a fan, that then leads to a T-split where air distributes to the primary and secondary annular channels. Presently there are no measurement data available on the distribution of air between primary and secondary channels. Thus, in order to determine inlet boundary conditions, a preliminary CFD study was performed on the air section upstream of the burner using the total air mass flow rate derived from stoichiometry in Section 3.2.

The simulated geometry consists of a single inlet pipe of diameter $d = 70$ mm, feeding into a T-junction which splits the flow into two horizontal branches. Each branch leads into a cylindrical transition chamber, from which the flow enters the respective annular channel of primary or secondary air. The transition chambers have heights of 86 mm and 92 mm for the primary and secondary air respectively, with an identical outer diameter of 240 mm. A development length of $10d = 700$ mm was applied at the inlet and at each T-junction branch. The primary annular channel is extended by 92 mm relative to the secondary due to the transition chambers being stacked, resulting in channel lengths of 413 mm and 321 mm for primary and secondary respectively, based on $10D_h$ of the secondary channel ($D_{h,2} = 32.1$ mm). However, simulations were also performed with equal channel lengths for primary and secondary, and the difference of this extra length was found to be negligible with less than 1% difference.

Table 3.4 presents the results found of the air distribution. Simulations were performed with two different models, realizable $\mathrm{k}-\varepsilon$ with non-equilibrium wall treatment and $\mathrm{k}-\omega$ SST, more detailed explanation of these models and options can be seen in Section 2.1. This was in order to determine model independence due to the difficulty in ensuring proper y^+ in the geometry.

Table 3.4: Air distribution study results of primary/secondary air.

Model	No fins	With fins
$\mathrm{k}-\varepsilon$	29.5/70.5	24.1/75.9
$\mathrm{k}-\omega$	29.0/71.0	24.4/75.6

The fins shift the air split noticeably towards the secondary channel, from approximately 29/71 without fins to 24/76 with fins, reflecting the additional pressure drop induced by the primary swirl fins. The two turbulence models agree to within 1%, indicating that the result is not sensitive to the model choice. The larger fraction in the secondary channel is consistent with its larger cross-sectional area and lower

flow resistance. As the result obtained with the fins included is more physically representative, it is carried forward as the basis for inlet conditions for primary and secondary air. Given that the split is a CFD prediction rather than a measurement, the result is treated as indicative and rounded to 25/75 for use as the inlet boundary condition.

3.5 Lance Inlet Condition Study

The propane and hydrogen cases share the same primary and secondary air channels, and both represent these as annular face inlets rather than resolving the swirl fins. Standard inlet turbulence correlations assume fully-developed pipe flow and do not reflect the elevated turbulence levels generated by the swirl fins. A preliminary CFD study of the fuel lance was therefore performed to extract representative turbulence quantities for use as inlet boundary conditions. Turbulence intensity and turbulent viscosity ratio were used, since the viscosity ratio avoids the need to define a hydraulic diameter, which is not straightforward for the finned annular channels. The simulated geometry resolved the full three-dimensional fuel lance, including the primary and secondary swirl fins, as shown in Figure 3.3. The inlet channels were extended by 240 mm upstream of the lance exit to allow for profile development. Downstream of the lance, the flow expanded into a cylindrical volume of diameter 200 mm and length 600 mm, sized to suppress backflow at the outlet boundary.

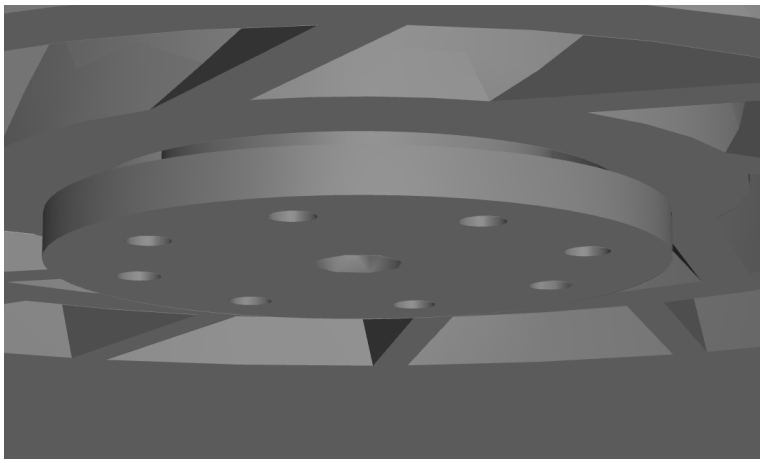

Figure 3.3: Close-up view of the simulated fuel lance plate. The primary air swirl fins are visible around the perimeter.

The simulation was performed using the Reynolds Stress Model (RSM), chosen for its ability to capture the anisotropic stresses associated with the swirling flow around the lance (Section 2.1.3). The area-weighted averages of turbulence intensity and

turbulent viscosity ratio at the primary and secondary annular exits were used as inlet boundary conditions in the full cases for propane and hydrogen. The simulation also indicated that the annular gap carries the majority of the propane flow at approximately 73%, with the remaining 27% distributed across the eight perimeter holes, consistent with the larger effective injection area of the gap.

3.6 Propane Case

The modeling of the propane case represents the furnace as one quarter of its 3D domain, using 90° periodicity. The domain included a short annular propane pipe segment leading to the plate geometry and the cone. The hydrogen channel was excluded in this case in order to simplify the computational domain as a preliminary simulation with and without the channel showed negligible difference in the flow field immediately downstream of the burner. The air channels were simplified to be annular face inlets with their respective dimensions presented in Table 3.3 and the outlet was simplified to be axially located at the bottom of the furnace instead of on the side of the furnace wall as shown in Figure 3.1. Initial models used the full 3D domain, however it was found that the flow becomes unsteady due to the strong swirl of primary air, causing a precessing vortex core - a helical vortex rotating around the centerline at a characteristic frequency [6]. To aid flame stabilization, the experimental setup includes a cone at the end of the fuel lance, which is also included in the simulation domain. No detailed measurements of the cone geometry were available, and its dimensions were estimated from the available schematic. While the cone helped stabilize the flow, the solution still showed unsteady characteristics at higher-order discretization schemes. In reality, unsteady physics should be modeled with an unsteady model, such as unsteady Reynolds-averaged Navier-Stokes (URANS). However, due to the complex geometry of the fuel lance and the stiffness inherent to fast chemistry, the time-step that would be required needs to be small, causing the solution to be time-demanding. Due to time limitations, the quarter domain was modeled instead to force the vortex to be localized at the centerline, removing its frequency-dependent fluctuation and enforcing a time-steady solution.

The mesh was constructed using polyhedral cells. Polyhedral cells were chosen primarily because the flow lacks a dominant direction due to the swirl, and the cone requires unstructured cells to capture the geometry. Since the flow is not normal to the cell faces, some numerical diffusion will be present, which raises the importance of higher-order discretization schemes. Polyhedral cells help mitigate this by filling a given domain with fewer cells than tetrahedral or hexahedral meshes while providing more neighbors per cell, which improves gradient reconstruction [14]. Care was taken in modeling the small details in the lance geometry such as the gap and the holes by using smaller, localized cells in these regions. Additionally, the mesh was also refined in the flame region compared to the rest of the furnace domain. During mesh construction, particular care was taken to limit cell aspect ratio and to smooth size transitions.

Inlet conditions were set in accordance to the operating conditions described in Sec-

tion 3.2. Swirl for the primary and secondary air inlets was induced by specifying direction vectors with axial and tangential components, calculated from the prescribed swirl numbers in Table 3.3. For each inlet, the axial velocity was obtained from the prescribed mass flow rate, gas density and annular cross-sectional area. The tangential component u_θ was calculated from the corresponding swirl number using equation 2.10, and by assuming uniform velocity profiles across the inlet:

$$\bar{u}_\theta = \frac{3}{2} \cdot \frac{(R_o^2 - R_i^2)\, R_o}{R_o^3 - R_i^3} \cdot S \cdot \bar{u}_z \tag{3.6}$$

The resulting velocity components correspond to equivalent fin angles of $\arctan(u_\theta/u_z) = 43.4°$ for the primary inlet ($S = 0.79$) and $14.1°$ for the secondary inlet ($S = 0.21$), in close agreement with the design fin angles of 45° and 15°. This consistency supports the derivation of Equation 3.6 from the annular form of the swirl number.

With u_z and u_θ established, the mass flow rate at each annular inlet was assigned from the air distribution result (Section 3.4), and the inlet flow direction was specified as a unit vector with components $u_z/|u|$ and $u_\theta/|u|$, where $|u| = \sqrt{u_z^2 + u_\theta^2}$.

Wall boundary conditions were set as fixed temperatures (Dirichlet). The experimental campaign included cooling rods at the side walls that extracted heat from the system, and these are not included in the simulated geometry (Section 3.1). To partially account for the heat extraction by the cooling rods, the average of the measured gas temperatures at -400 mm across ports M2-M5 (Appendix A.1), the outermost radial position available across all four ports, was applied uniformly to the side wall. The cone, for which no temperature measurements were available, was assigned a fixed temperature of 1500 K. This value was chosen to provide some heat in the near-burner region to aid the kinetics, while remaining below the centerline gas temperature of 1818 K measured at the M2 port.

The Realizable $k - \varepsilon$ turbulence model described in Section 2.1.1 was used. Ideally RSM would be used due to anisotropy in the highly swirling flow, however, due to the increased complexity the model was not able to converge when applying higher-resolution mesh coupled with chemistry interactions. The combustion chemistry was represented by EDC described in Section 2.3.4 with two different global reaction mechanisms tested: two-step Westbrook and Dryer and four-step Jones and Lindstedt, which are described in Section 2.3.5. A comparison simulation that used the ED model was also performed with the 2-step mechanism that excluded the reversible step. Radiation was accounted for with the DOM model described in Section 2.4.1, the default angle discretization of $M_\varphi = 2$ and $M_\theta = 2$ was applied and DOM was coupled with WSGGM described in Section 2.4.2. Fluent's built in WSGGM was used and is based on work done by Smith et al. [15]. The internal emissivity was set to unity. The refractory lining of the furnace has a material emissivity of approximately 0.9, however, at thermal steady state the rate of emission and absorption at the wall surface must balance, resulting in an effective emissivity of unity regardless of material properties [16]. The pressure-based pseudo-transient solver with coupled scheme was used. The discretization scheme for the pressure was PRESTO!, the rest used second-order upwind scheme.

A mesh sensitivity study was performed under cold-flow conditions. Three mesh resolutions were tested: 199k, 242k, and 315k cells. Outlet velocity magnitude differences were 2.8% between the 199k and 242k meshes, reducing to 0.5% between the 242k and 315k meshes, indicating asymptotic convergence. Mass balance closed to better than 3e-7 kg in all cases. The 242k cell mesh was selected as the working mesh with reacting simulations as a compromise between solution accuracy and computational cost.

3.7 Hydrogen Case

The hydrogen case used mostly the same configuration as the propane case. The differences were that this configuration does not use a cone, to reflect the new burner configuration that is under development. Additionally, this new configuration will not include any cooling tubes, the walls are instead treated as adiabatic. The lance geometry as seen in Figure 3.2 is modified in this case to exclude the propane channel, gap and holes, instead only the centrally located hydrogen channel is considered, in line with the methodology used for the propane case.

The 1-step global mechanism $H_2 + 0.5\,O_2 \longrightarrow H_2O$ using ANSYS Fluent default Arrhenius parameters ($A = 9.87 \times 10^8$ $m^3\,kmol^{-1}\,s^{-1}$, $E_a = 31$ $kJ\,mol^{-1}$) was used. For propane, the two-step Westbrook-Dryer mechanism is the minimum description capable of representing the CO intermediate and the coupled heat-release distribution between the fast partial-oxidation step and the slower CO-to-CO_2 conversion. Hydrogen combustion contains no corresponding stable intermediate species. H_2 oxidation in air proceeds through short-lived radicals which would require a reduced or detailed kinetic scheme to capture, for example the 7-step Baurle mechanism. Such a mechanism would provide improved fidelity at the cost of computational time. For the present work the quantities of interest are mainly centerline and radial profiles of temperature and major species, and flue gas composition at the furnace outlet. These are primarily determined by the overall heat release, stoichiometry between fuel and oxidizer, and the turbulent mixing field; the 1-step global mechanism is considered adequate.

3.8 Plasma Case

The quarter domain adopted in the propane (Section 3.6) and hydrogen (Section 3.7) cases was also used for the plasma case. The inlet channel does not use the same lance as the aforementioned cases. Instead, the lance is replaced with a plasma heating configuration. In reality, the plasma torch geometry and arc physics are complex, and require substantial modeling efforts to capture. A simplified representation was therefore adopted: the plasma heater is modeled as a cylindrical channel split into three axial segments representing the cathode, the heated source region, and the anode, with pure CO_2 entering the upstream face. A uniform volumetric heat source is applied to the source region, representing the energy supplied by the arc. A schematic of the configuration is shown in Figure 3.4. This simplification preserves the total energy deposited into the gas and the approximate axial length

over which it is deposited, but the localized energy profile of the arc is lost. Because the heating occurs upstream of the furnace, hot, partially dissociated gas enters the furnace domain, in contrast to the propane and hydrogen cases where combustion takes place inside the furnace.

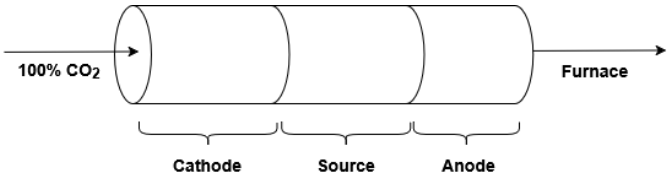

Figure 3.4: Schematic overview of how the plasma burner was modeled.

The source region has a length of $L_{\text{source}} = 53\,\text{mm}$ and a diameter of $D_h = 18\,\text{mm}$, with the cathode segment approximately 24 mm and the anode approximately 123 mm. Source and anode length was estimated from a schematic of the reference torch design, cathode length was shortened deliberately to minimize domain size. The mass flow rate from Section 3.2 was applied at the inlet at 298.15 K. The volumetric heat source applied to the source region was $2.91\times10^{9}\,\text{W m}^{-3}$, corresponding to the 40 kW load. The source term was ramped over the first iterations via a user-defined function to improve numerical stability during start-up; the ramp affects only the transient path to convergence.

Similar to the propane and hydrogen cases, extra mesh-refinement was applied in critical regions: the cylindrical representation of the plasma heater and injection zone of heated gas into the furnace, with subsequently coarser mesh in the bulk furnace. The mesh size was aimed to be of similar resolution to that of the propane and hydrogen cases, resulting in ~260 thousand cells for the quarter domain. The mesh was constructed with poly-hexcore that uses hexahedral cells in the center-bulk and polyhedral cells near the walls, in contrast to the other cases which used purely polyhedral cells. This option was chosen due to the simpler geometry and absence of swirling flow.

The same turbulence settings were used as in the propane and hydrogen cases, with walls treated as adiabatic like in the hydrogen case. The dissociation of CO_2 was treated using the Eddy Dissipation Concept (EDC) model (Section 2.3.4). A reduced reaction mechanism for CO_2 dissociation, supplied in CHEMKIN format with corresponding thermodynamic data, was used with species O, O_2, C, CO, CO_2 and N_2. The thermodynamic data is valid up to 5000 K; cell temperatures were limited to this value to avoid extrapolation of the polynomial fits outside their validity range.

Radiation was modeled with the DOM (Section 2.4.1) coupled with a WSGGM formulation (Section 2.4.2) implemented through user-defined functions for the band absorption coefficients and emissivity weighting factors. The WSGGM parameters were taken from Ehlmé et al. [17], who provide CO_2 and H_2O radiative property data valid up to 5000 K. This range matches the validity limit of the thermodynamic data and makes the formulation suitable for the elevated temperatures present in the plasma case.

4

Results and Discussion

This chapter presents and discusses the simulation results. The propane case is examined first and compared against the experimental reference data introduced in Section 3.1, focusing on the influence of the turbulence-chemistry model and the reaction mechanism. The validated modeling framework is then applied to the hydrogen and plasma cases, for which no direct experimental counterpart is available, and the two are compared to characterize how the heating approach affects the thermal and chemical behavior.

4.1 Propane Case Results

Three model combinations were run for the propane case: the eddy-dissipation (ED) with the Westbrook-Dryer (WD) two-step mechanism without reversible reaction, the eddy-dissipation concept (EDC) model with the two-step Westbrook-Dryer mechanism with reversible reaction enabled and EDC with Jones-Lindstedt (JL) mechanism. Centerline axial profiles of temperature and dry-basis species mole fractions are compared against the port measurements at M2-M5, with M6 included for the species profile as an indicative reference (Section 3.1).

Figure 4.1 compares the centerline temperature predicted by the three model combinations against the measured temperatures at the axial position in ports M2-M5. Comparing ED against EDC, the ED model predicts a smooth, gradual temperature rise that begins near the inlet, reaches a broad peak and decays slowly towards the outlet. The ED model shows good results for anchoring the flame indicated by the immediate temperature rise, but under-predicts the peak and shows temperatures consistent with an over-extended flame. This behavior is consistent with the ED model assigning the same turbulent rate to all reactions in the mechanism, producing an early and distributed heat release rather than a localized flame.

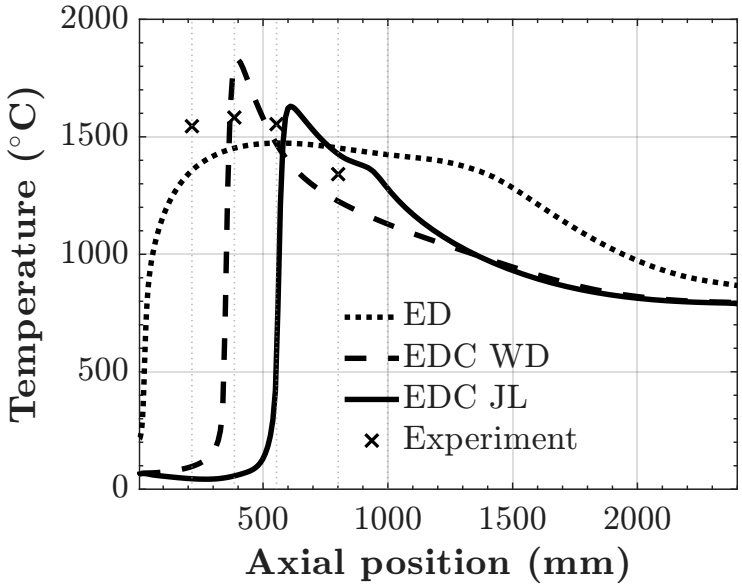

Figure 4.1: CFD-predicted temperatures along the centerline for ED using 2-step mechanism without reversible reaction, 2-step Westbrook and Dryer mechanism with EDC, and 4-step Jones-Lindstedt mechanism with EDC against the measured experimental temperature.

Both EDC variants show delayed ignition with a sharp increase in temperature at roughly 300 mm for WD and roughly 500 mm for JL. Both exhibit a sharp peak that over-predicts temperature with WD peak being more pronounced. The WD mechanism anchored closer to the burner compared to JL. The EDC variants capture the flame length more accurately as the decrease in temperature occurs earlier than what ED predicts. EDC WD manages to predict temperatures at M3, M4 and M5 fairly well, whereas JL only manages to be close to M4 and M5. Excluding M2, the EDC WD model reproduces the centerline temperature with a mean absolute error of 140 °C (9.3%), with the largest deviation at M3 where the model over-predicts by ~14%, reducing to ~5% at M4 and ~9% at M5. The main deficiency in the EDC predictions is that the flame is lifted and does not anchor properly, instead stabilizing further downstream.

The cause for the lifted flame was not determined. The observation that the more detailed JL mechanism produces more pronounced lift-off than WD under the same turbulence model points to chemistry as a contributing factor. Both mechanisms lack radical chain-branching reactions, which play a role in the ignition, and post-processing of the EDC timescales shows that they are shortest in the lift-off region, suggesting that the global kinetics are too slow to sustain ignition there. Including fast-reacting radical steps could plausibly allow the flame to anchor closer to the burner. Two further contributors cannot be ruled out: the as-built swirl may deviate from the design values used as inlet conditions (Section 3.3), and the steady quarter-domain treatment cannot represent the precessing vortex core observed in the preliminary full-domain simulations (Section 3.6). The relative impact of possible contributors considered is estimated in Table 4.1.

Table 4.1: Potential contributors to the predicted flame lift-off, listed in estimated order of impact.

Contributor	Description
Global mechanism	No radical chain-branching reactions; ignition chemistry too slow in the near-burner fine structures.
Transient physics	Quarter-domain forces a steady-state solution, suppressing the precessing vortex core that may aid flame stabilization.
Swirl uncertainty	As-built fin angles may deviate from the design values used as inlet conditions.
Cone temperature	Estimated at 1500 K without measurements; minor effect based on preliminary sensitivity.

If the flame were to anchor earlier, the close agreement at M3-M5 could potentially shift, given the sharp temperature gradients the mechanisms predict. Such a case could possibly be remedied by setting a more refined wall boundary condition, as the current boundary condition is based on uniform mean gas temperature measurements in close proximity to the wall as presented in Section 3.6. Another boundary condition could instead utilize a temperature profile based on these measurements, which shows increased gas temperature from M2 to M5, however a potential shortcoming of such a method is that there is no validation data from the same campaign past the M5 port, and as such unvalidated temperatures would have to be set past the M5 port.

Figure 4.2 show the radial temperature profiles for the two-step comparison at ports M3-M5. M2 was excluded due to the lift-off, and further discussion in relation to the radial distribution would not add value. Since the WD model showed the best agreement, the other models are omitted.

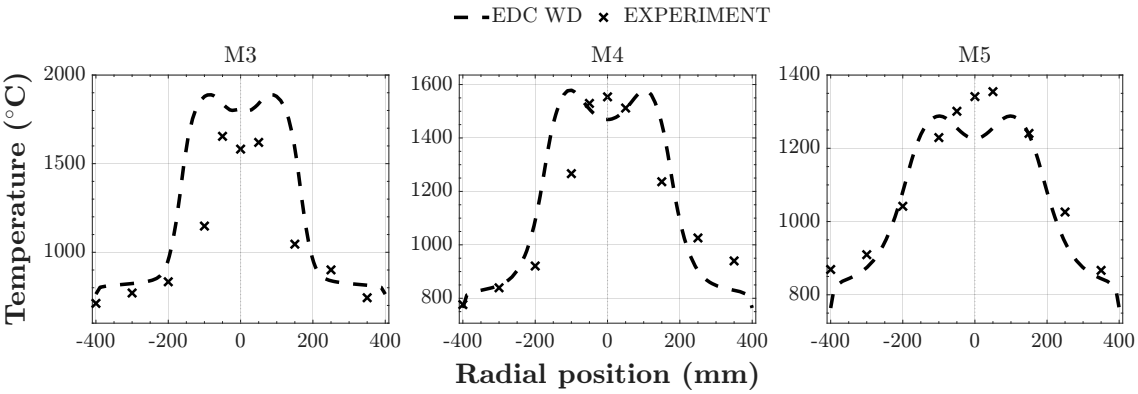

Figure 4.2: Radial temperature profiles at ports M3, M4 and M5 predicted from EDC using 2-step Westbrook-Dryer compared against experimental data.

The radial profiles show that WD EDC predicts the qualitative shape at M3, but over-predicts the magnitude as is consistent with Figure 4.1. At M4 the simulation

matches experimental value on the centerline, but shows a double peak not present in the validation data. Wall temperature at the negative radial coordinates matches well, but under-predicts the validation data at positive radial coordinates. The experimental data appears to have some asymmetry which might be attributed to measurement variability. M5 shows good agreement overall but under-predicts the peak, showing consistent double peak behavior. The double peak behavior may be exaggerated relative to the measurement: the suction pyrometer used in the experimental campaign measures a small sample volume, effectively averaging over local gradients. In contrast the simulation samples point values along the radial lines. The EDC WD combination therefore captures the bulk flame structure from M3 onwards but does not reproduce the near-burner region, which is taken as a known limitation when interpreting the species results that follow.

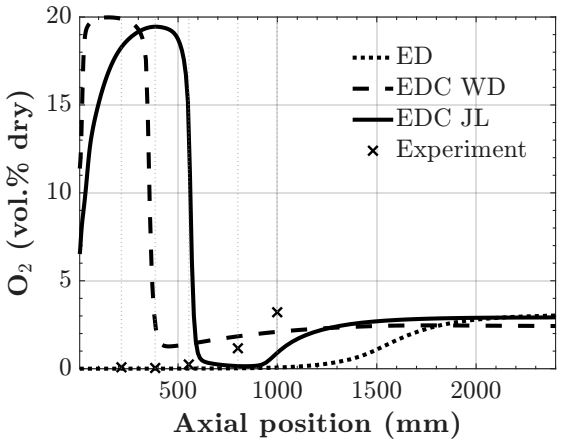

(a) O_2 mole fraction along the centerline.

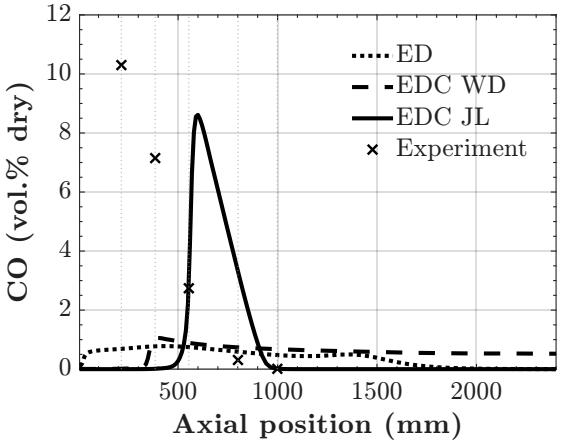

(b) CO mole fraction along the centerline.

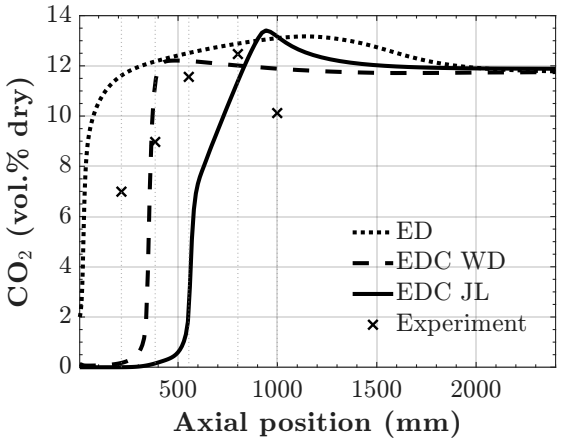

(c) CO_2 mole fraction along the centerline.

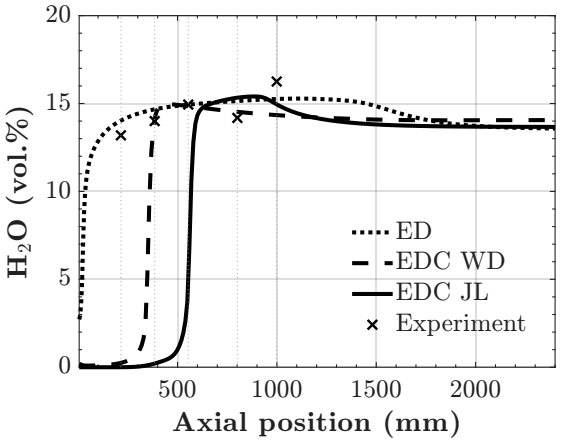

(d) H_2O mole fraction along the centerline.

Figure 4.3: Centerline mole fraction profiles of major species for the propane case using ED with the 2-step Westbrook-Dryer mechanism (ED), EDC with the 2-step Westbrook-Dryer mechanism (EDC WD), and EDC with the 4-step Jones-Lindstedt mechanism (EDC JL), compared against measurements at ports M2-M6.

Figure 4.3 shows the centerline mole fractions for the three models tested and compare them against available experimental data. Lift-off is perhaps best presented in Figure 4.3a, where there is a clear over-prediction of O_2 by the EDC models since the combustion has not started. The JL mechanism produces the best qualitative shape consistently (M6 experimental data is not from the same campaign), but the pronounced lift-off is reflected by its axial offset. For CO predictions, JL is observed to be the only mechanism capable of reproducing the experimental peak magnitudes, although it under-predicts the magnitude by roughly 1 percentage point.

The WD mechanism retains CO at the outlet while the ED model's CO declines downstream. In both models R1 produces CO and R2 consumes it, the difference is in the downstream behavior of R2. In WD R2 is reversible, allowing CO_2 to dissociate back to CO at elevated temperatures and sustaining the CO level. In ED model R2 is irreversible, so once R1 ceases to produce CO as the propane is consumed, R2 continues to deplete the remaining CO without any possibility for regeneration. The JL mechanism also has a reversible CO step (R4), but the water-gas shift reaction depends on H_2O rather than O_2. By Le Chatelier's principle, the abundance of H_2O in comparison to O_2 downstream (~14% compared to ~3%) drives this equilibrium towards CO_2. The ED model appears to compare favorably in the H_2O prediction, reflected by its ability to ignite closer to the burner caused by its simplified mixing-limited mechanism. Taken together, this suggests that it is likely that the EDC models are kinetically limited in the near-burner region.

The radial profiles of O_2, CO, CO_2 and H_2O are presented for both EDC variants. The comparison reveals mechanism-specific features that the centerline plots do not fully resolve.

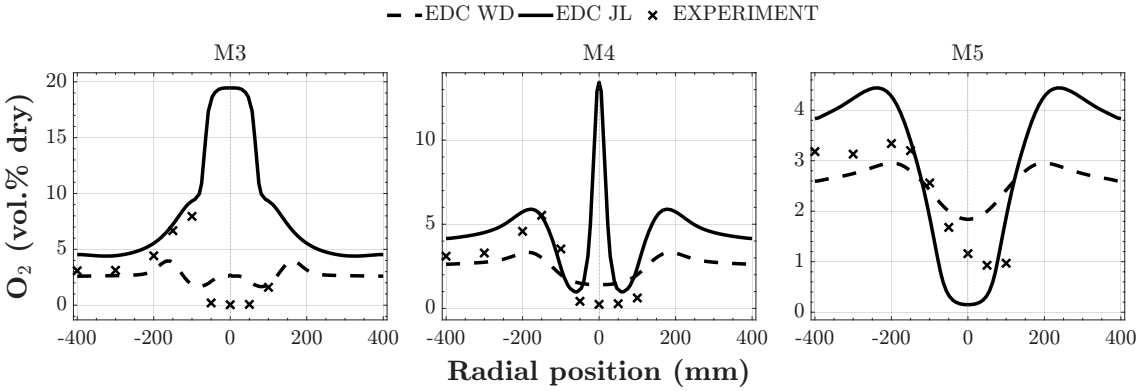

Figure 4.4: Radial O_2 profiles predicted by EDC using 2-step Westbrook-Dryer and 4-step Jones-Lindstedt mechanism.

The radial O_2, CO, CO_2 and H_2O profiles (Figures 4.4, 4.5, 4.6, 4.7) show two distinct behaviors between the mechanisms. The WD mechanism predicts flat radial profiles across all ports and species, which do not capture the pronounced peaks and troughs in the experimental data. The JL mechanism produces sharper radial gradients across all ports, aligning in shape with the experimental gradients in O_2 at M4 and M5, but overshoots in magnitude particularly at M3 where the lift-off amplifies the discrepancy. JL also produces non-negligible CO levels at M4 and M5

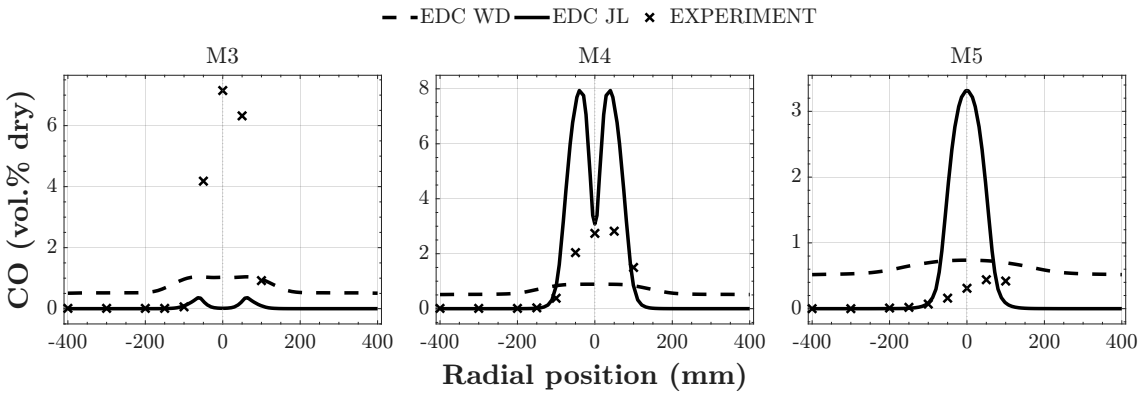

Figure 4.5: Radial CO profiles predicted by EDC using 2-step Westbrook-Dryer and 4-step Jones-Lindstedt mechanism.

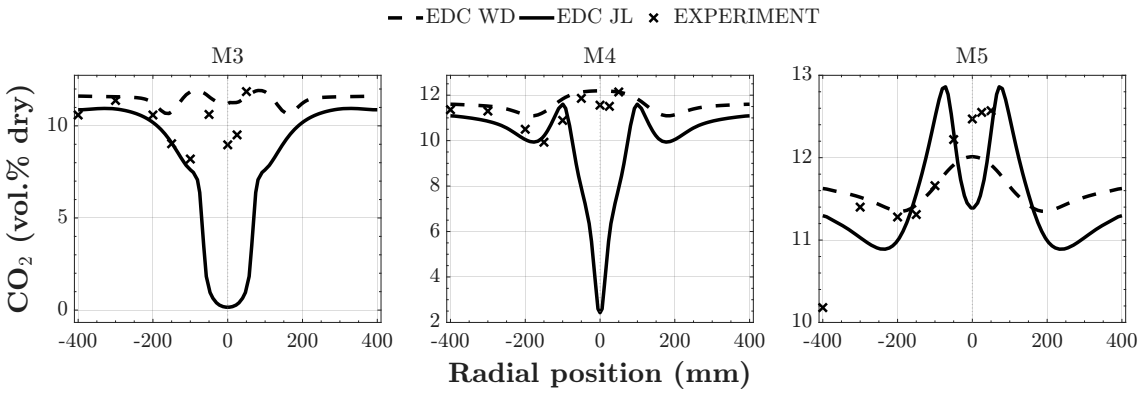

Figure 4.6: Radial CO_2 profiles predicted by EDC using 2-step Westbrook-Dryer and 4-step Jones-Lindstedt mechanism.

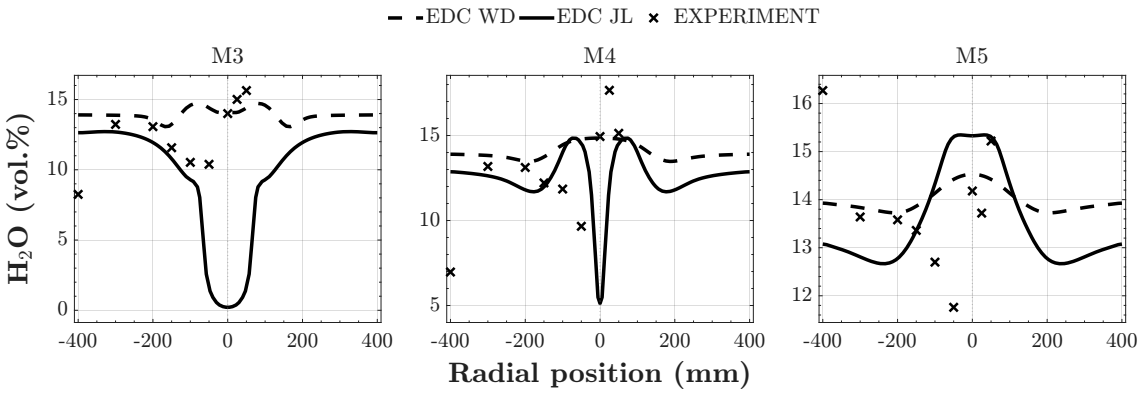

Figure 4.7: Radial H_2O profiles predicted by EDC using 2-step Westbrook-Dryer and 4-step Jones-Lindstedt mechanism.

where WD predicts near-zero CO, consistent with the mechanism's retention of CO as an intermediate species. Neither mechanism is uniformly better across the major species, but JL's gradient handling indicates that it would more closely capture the radial profile shapes where the experiment has clear peaks and troughs, if the flame anchoring were correctly predicted.

Table 4.2: Area-weighted average flue gas composition at the outlet for the three model combinations, compared against the stoichiometric composition for complete combustion of propane at $\dot{m}_{\text{fuel}} = 1.73\ \text{g}\,\text{s}^{-1}$ and $\lambda = 1.15$ (Table 3.1).

Case	O_2 [%wet]	O_2 [%dry]	CO_2 [%wet]	CO_2 [%dry]
Stoichiometric	2.55	2.95	10.21	11.82
ED	2.63	3.04	10.17	11.77
EDC WD	2.03	2.36	10.13	11.79
EDC JL	2.54	2.95	10.25	11.87

The area-weighted average flue gas composition at the outlet is presented in Table 4.2 for the three model combinations and compared against the stoichiometric composition from Table 3.1. The ED and EDC JL predictions match the stoichiometric values within approximately 0.1 percentage points across all four columns. The EDC WD prediction shows an O_2 deficit of approximately 0.6 percentage points on a wet basis (2.03% versus 2.55%), consistent with the residual centerline CO retained by this mechanism (Figure 4.3b). The CO_2 values are consistent across all three models within 0.1 percentage points of the stoichiometric expectation. The global mass and atom balance is therefore well preserved, despite the local differences in flame structure and species composition discussed above.

The propane case provides validation of the modeling framework against experimental data. From M3 onward, the EDC predictions capture the bulk temperature and major species structure reasonably well, and the area-weighted outlet composition is consistent with the stoichiometric expectations across all models. The main deficiency is the lifted flame, which prevents the near-burner region at M2 from being captured. Isolating the contributions listed in Table 4.1 would require a transient simulation of the full domain with an extended reaction mechanism, which was outside the scope of the present work due to the computational cost of the coupled chemistry and complex lance geometry.

The turbulence, radiation and combustion modeling framework validated here, namely the realizable $k - \varepsilon$ model, EDC, and DOM coupled with WSGGM on the quarter domain, is carried forward to the hydrogen and plasma cases. The mechanism comparison between the two-step and four-step models does not transfer to the hydrogen case, which contains no stable intermediate species and is represented with a single-step global mechanism (Section 3.7).

4.2 Hydrogen Case Results

Figure 4.8 shows the centerline temperature for the hydrogen case along the full furnace length, with ports M2 through M7 marked. In contrast to the propane case, the hydrogen flame anchors immediately at the burner, with the centerline temperature rising steeply from the inlet and reaching approximately 1500 °C by M2. The temperature peaks at approximately 2230 °C near M4 before decaying to a plateau of approximately 1800 °C toward the outlet. This peak is likely an over-prediction, as the single-step mechanism releases all combustion heat in a single reaction without representing the dissociation of products at high temperature that would moderate the peak temperature in reality.

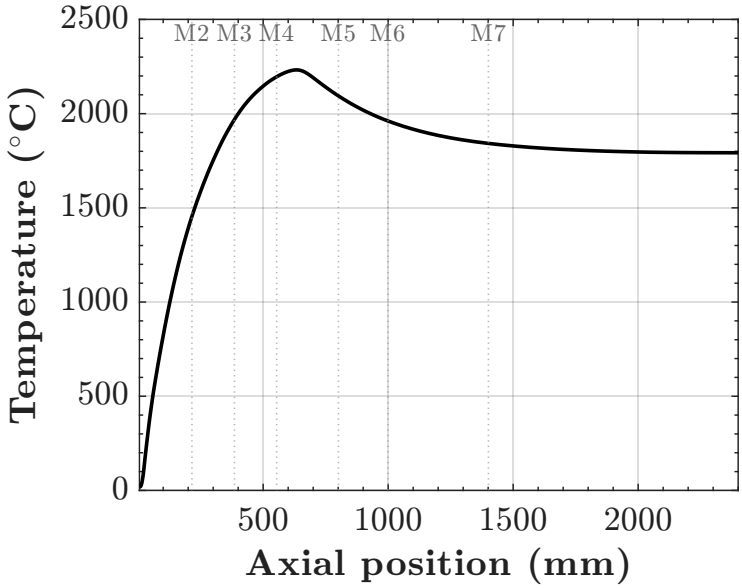

Figure 4.8: CFD-predicted temperature of H_2-combustion along the centerline using 1-step mechanism with the EDC model.

The absence of lift-off may reflect the faster kinetics of hydrogen combustion, the single-step mechanism used, or a combination of both. The elevated outlet temperature, compared to approximately 800 °C in the propane case, is a consequence of the adiabatic wall treatment (Section 3.7), which removes the wall heat extraction present in the propane configuration.

The radial temperature profiles at ports M3 through M6 are shown in Figure 4.9. Radial plots for ports M2 and M7 are available in Appendix A.2. M3-M6 were selected as these capture the evolution of the flame development, with M2 and M7 reflecting the profiles for M3 and M6 respectively.

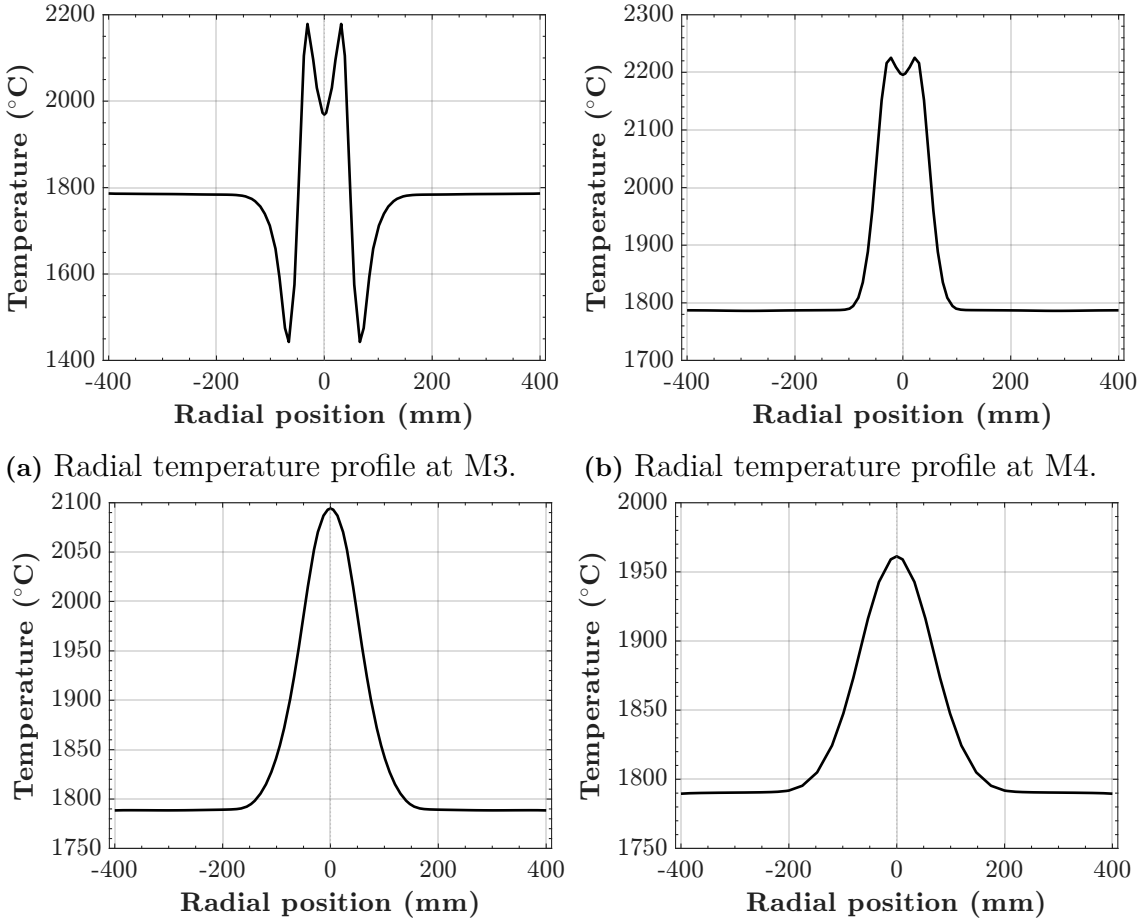

(a) Radial temperature profile at M3.

(b) Radial temperature profile at M4.

(c) Radial temperature profile at M5.

(d) Radial temperature profile at M6.

Figure 4.9: Radial temperature profiles at ports M3, M4, M5 and M6 predicted from EDC using 1-step mechanism for H_2-combustion.

Near the burner the profile at M3 in Figure 4.9 shows a double-peak structure, with two hot reaction zones at approximately ±30 mm, bounded by cold troughs at approximately ±60 mm corresponding to the unreacted air feeding in from the swirled annular channels. The centerline dips below the double-peak and corresponds to the central hydrogen jet which has not fully reacted at this position. As the flow moves downstream the cold air is progressively consumed: the troughs warm and disappear, and by M4 the double peak has largely merged. At M5 the double-peaks have merged into a single centerline peak, which then broadens and decreases in magnitude through M6 as the hot core mixes outward. Away from the reaction zone the gas sits at approximately 1800 °C throughout, consistent with the adiabatic walls and outlet plateau temperature of the centerline plot.

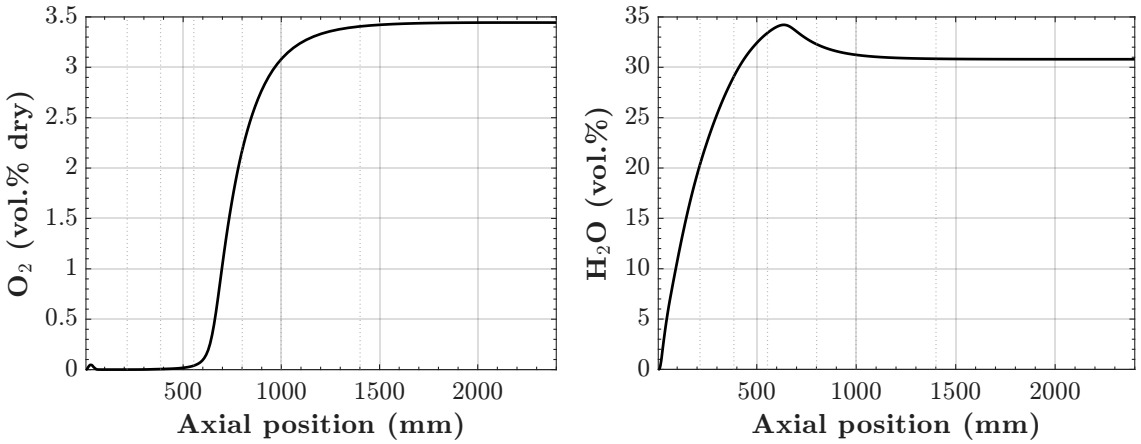

(a) O_2 profile along the centerline. **(b)** H_2O profile along the centerline.

Figure 4.10: CFD predicted O_2 and H_2O profiles of H_2-combustion along the centerline using 1-step mechanism with the EDC model.

The centerline mole fractions of O_2 and H_2O are shown in Figure 4.10. The O_2 profile remains near zero from the burner through approximately 600 mm, then rises to a plateau of approximately 3.4% (dry) toward the outlet. The near-zero O_2 in the near-burner region reflects the fuel-rich hydrogen jet on the centerline, where little oxidizer is present on the axis. As the central jet is consumed downstream and the excess air mixes inward, the O_2 rises to its outlet plateau. The H_2O profile has a steep rise starting near the burner, peaking at approximately 34% around 620 mm, coinciding with the centerline temperature peak, before settling to a plateau of approximately 31%. The location of the H_2O peak is consistent with the position of maximum reaction and temperature on the centerline.

The radial O_2 and H_2O profiles (Figures 4.11 and 4.12) reflect the same flame structure seen in the radial temperature. At M3 the O_2 profile shows a near-zero centerline, corresponding to the fuel-rich hydrogen core, flanked by sharp peaks of approximately 13% at $\pm$70 mm from the unreacted air jets. The H_2O profile is the inverse, with high values on the centerline and deep troughs at the same $\pm$70 mm positions where the unreacted air suppresses H_2O. As the flow moves downstream the air jets are progressively consumed: the off-axis O_2 peaks diminish and move outward, the centerline O_2 fills in from near zero at M3 to approximately 3.1% at M6, and the H_2O troughs fill in and shrink. By M6 both profiles are close to radial uniformity, suggesting that the combustion is largely complete and the zone is well-mixed towards the outlet as the profiles approach their bulk values of approximately 3.45% O_2 and 31% H_2O.

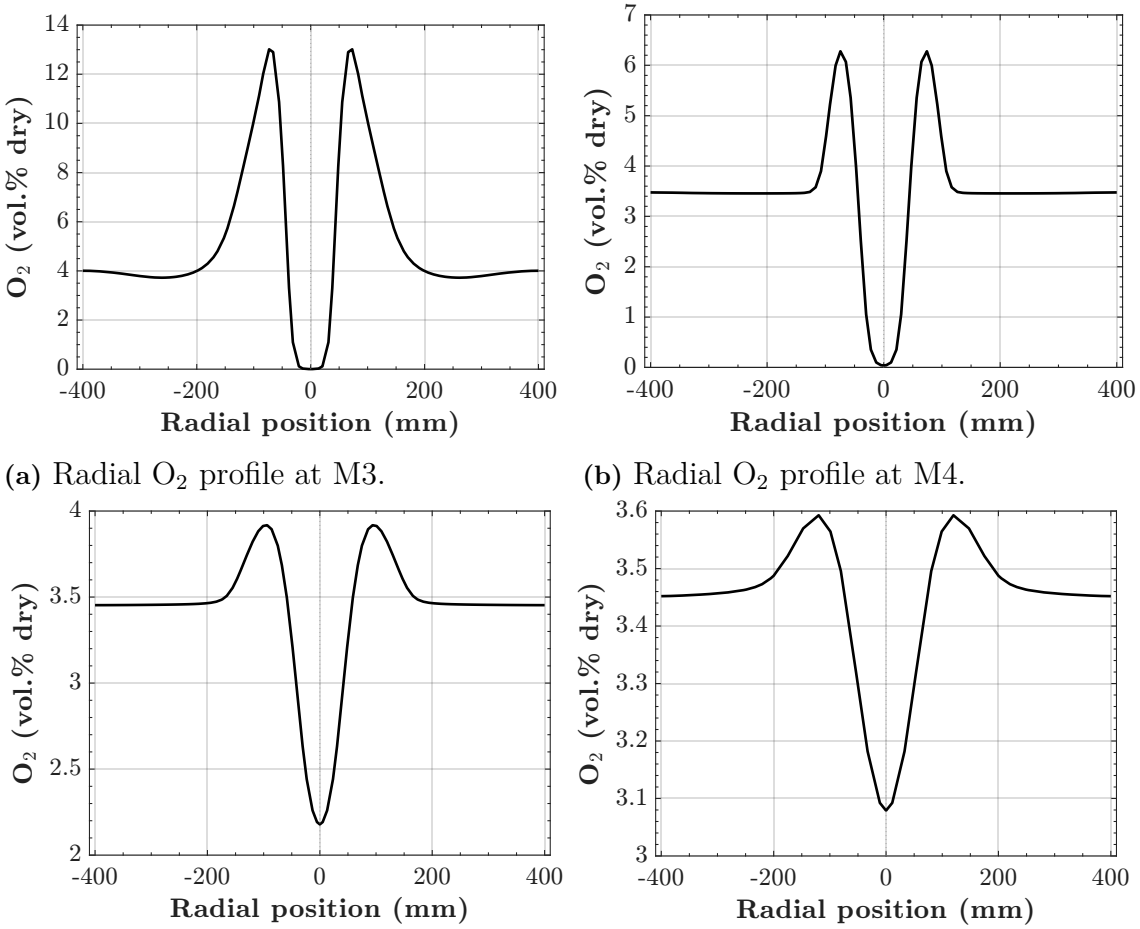

(a) Radial O_2 profile at M3.

(b) Radial O_2 profile at M4.

(c) Radial O_2 profile at M5.

(d) Radial O_2 profile at M6.

Figure 4.11: Radial O_2 profiles at ports M3, M4, M5 and M6 predicted from EDC using 1-step mechanism for H_2-combustion.

Table 4.3: Area-weighted average flue gas composition at the outlet for the hydrogen case, compared against the stoichiometric composition for complete combustion of hydrogen at $\dot{m}_{\text{fuel}} = 0.33\ \text{g}\,\text{s}^{-1}$ and $\lambda = 1.15$.

Case	O_2 [%wet]	O_2 [%dry]	H_2O [%wet]
Stoichiometric	2.32	3.35	30.9
EDC	2.38	3.44	30.8

The area-weighted average flue gas composition at the outlet is presented in Table 4.3, compared against the stoichiometric composition for complete combustion of hydrogen at $\lambda = 1.15$. The hydrogen mole fraction at the outlet is negligible, confirming complete combustion. The predicted O_2 and H_2O fractions agree with the stoichiometric expectation within approximately 0.1 percentage points, indicating that the global mass balance is well preserved.

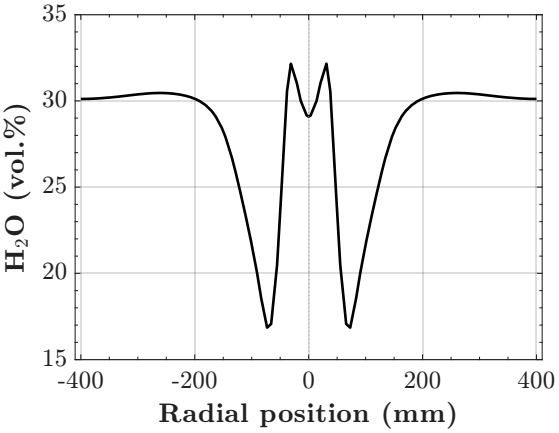

(a) Radial H_2O profile at M3.

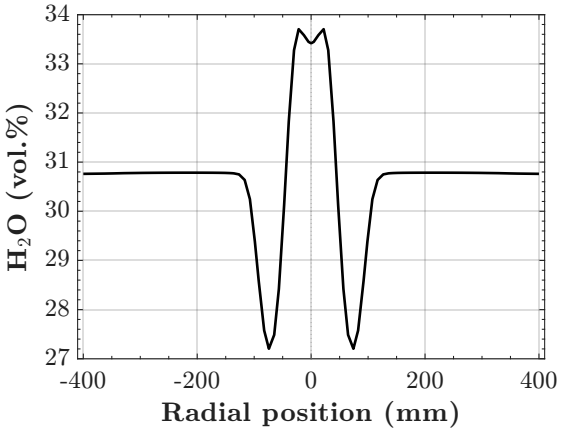

(b) Radial H_2O profile at M4.

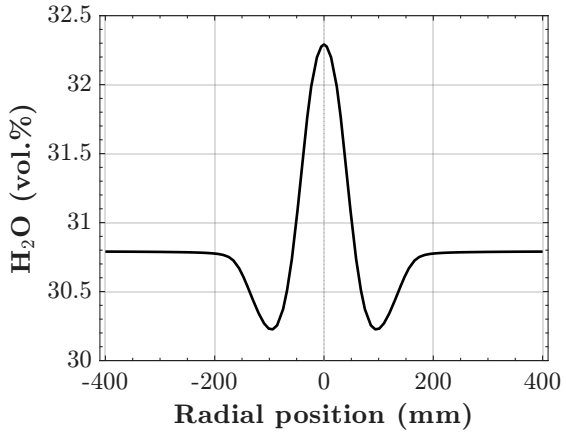

(c) Radial H_2O profile at M5.

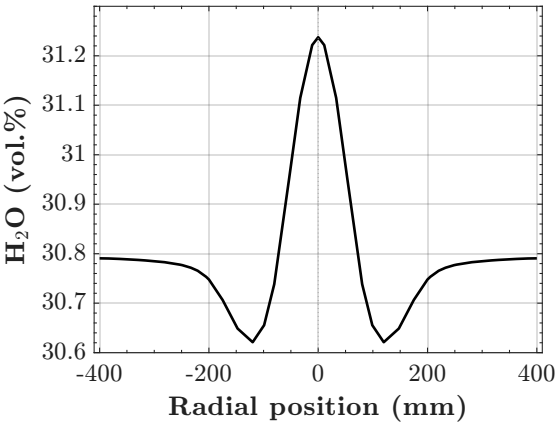

(d) Radial H_2O profile at M6.

Figure 4.12: Radial H_2O profiles at ports M3, M4, M5 and M6 predicted from EDC using 1-step mechanism for H_2-combustion.

4.3 Plasma Case Results

Figure 4.13 shows the centerline temperature through the furnace for the plasma case, from the furnace inlet to the outlet, excluding the upstream region where the plasma heating occurs.

In contrast to the propane and hydrogen cases, where the peak temperature occurs within the furnace at the flame, the plasma case reaches its maximum at the furnace inlet, since the energy is deposited upstream in the heater (Section 3.8). The gas enters the furnace at approximately 3020 °C and cools as it passes through the furnace, dropping steeply over the first ~100 mm. Downstream of this initial drop, the temperature recovers slightly as the exothermic recombination of the dissociation products releases heat, before settling to a nearly uniform plateau of approximately 2900 °C through the remainder of the furnace. This recombination is discussed further in relation to the centerline species plots (Figure 4.15). The elevated outlet temperature, higher than in the hydrogen case at the same 40 kW load, primarily reflects the smaller thermal mass of 4.91 $g\,s^{-1}$ of pure CO_2, compared to 13.4 $g\,s^{-1}$ of

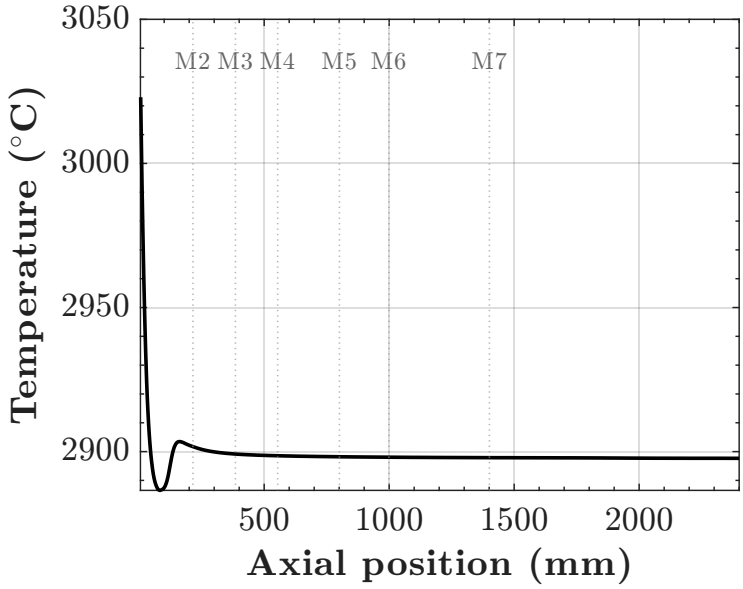

Figure 4.13: CFD-predicted centerline temperature for the CO_2-plasma case using the EDC model with a reduced CO_2 dissociation mechanism.

combustion products and air in the hydrogen case, so the same energy is distributed to a smaller mass flow.

The temperature clamp of 5000 K (Section 3.8) acts only in the heater source region upstream of the furnace, on ~0.6% of the total domain. It is necessary to clamp the temperature in this region to prevent the model from extrapolating thermodynamic data outside its validity range, which would likely result in unphysical results. The gas entering the furnace domain is well below this limit. The high source-region temperature is physically reasonable, as the energy is deposited into a small mass of pure CO_2, giving a high specific energy input in the source core. The uniform volumetric heat source and adiabatic walls direct all of the deposited energy into the gas. In the hottest cells the gas is rapidly heated CO_2 that has not yet dissociated, so the endothermic dissociation that would otherwise absorb part of the deposited energy has not yet taken effect in the cells where peak temperature is reported.

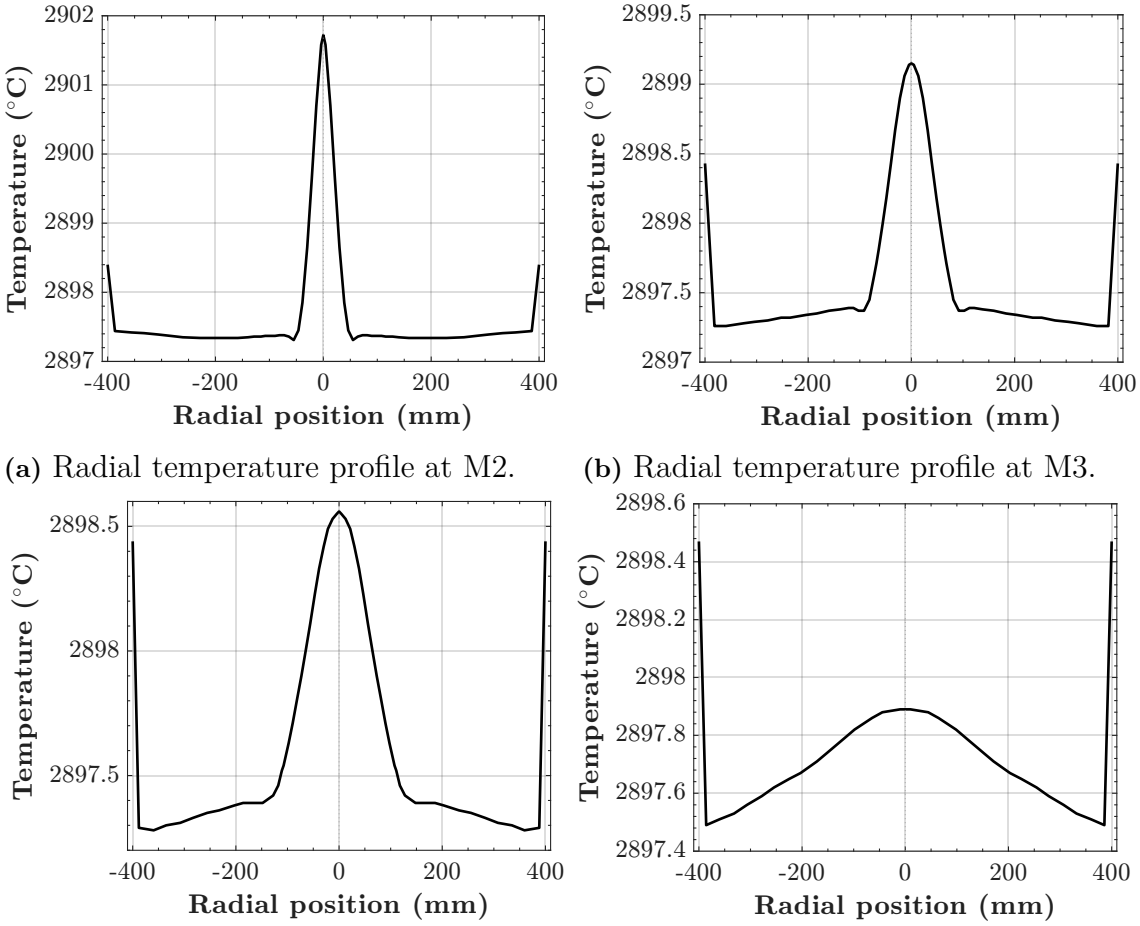

(a) Radial temperature profile at M2.

(b) Radial temperature profile at M3.

(c) Radial temperature profile at M4.

(d) Radial temperature profile at M7.

Figure 4.14: Radial temperature profiles at ports M2, M3, M4 and M7 predicted from EDC using a reduced CO_2 dissociation mechanism.

The radial temperature profiles at ports M2, M3, M4 and M7 are shown in Figure 4.14, with profiles at ports M5 and M6 excluded, as they follow the same trend. In contrast to the combustion cases, the profiles are nearly radially uniform: the total radial variation is approximately 5 °C at M2 and diminishes to less than 1 °C by M7, compared to approximately 2900 °C in the bulk temperature field. A narrow centerline peak is visible at M2 and M3, corresponding to the hot gas jet entering from the plasma heater channel. This feature broadens and diminishes downstream as the jet mixes into the surrounding gas. By M7 the profile is essentially flat. The high degree of radial uniformity reflects the absence of any reaction zone or cold air feed within the furnace, together with the adiabatic walls.

The centerline mole fractions of O_2, CO, CO_2 and O are shown in Figure 4.15. Atomic carbon was present only in trace amounts (peak at approximately 2×10^{-9} near the source) and is not shown.

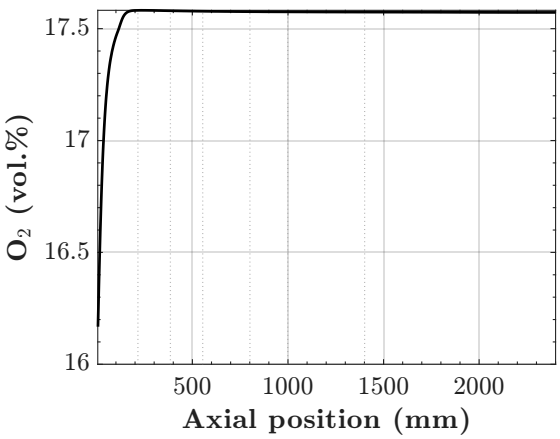

(a) O_2 mole fraction along the centerline.

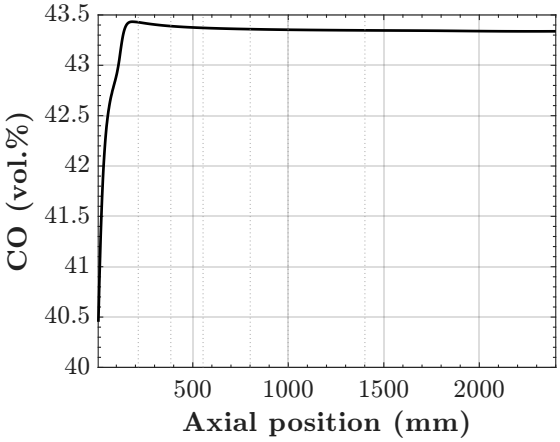

(b) CO mole fraction along the centerline.

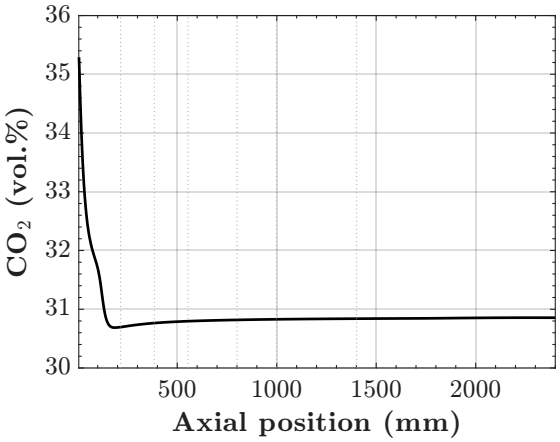

(c) CO_2 mole fraction along the centerline.

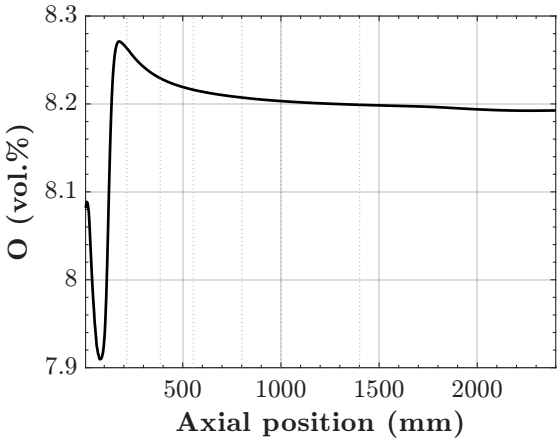

(d) O mole fraction along the centerline.

Figure 4.15: Centerline mole fraction profiles of species for the plasma case predicted from EDC using a reduced CO_2 dissociation mechanism.

The gas enters already substantially dissociated with CO at approximately 40.5%, O_2 at approximately 16.2%, O at approximately 8.1%, and CO_2 at approximately 35.2%. Over the first ~100-200 mm, dissociation continues as the chemistry catches up with the rapid upstream heating (the inlet state is under-dissociated relative to equilibrium, see Appendix A.4): CO_2 decreases while CO and O_2 increase. Beyond this region the composition stabilizes at approximately 30.8% CO_2, 43.5% CO, 17.6% O_2 and 8.2% O, with the CO_2 and CO profiles mirroring each other, suggesting that equilibrium has been reached. The ongoing endothermic dissociation in the first ~100 mm coincides with the temperature dip visible in Figure 4.13. Once equilibrium is reached the net energy absorption ceases and the temperature recovers.

To verify that the stabilized composition corresponds to chemical equilibrium, it was compared against the equilibrium composition of dissociated CO_2 at the bulk furnace temperature, computed by Gibbs free energy minimization (Appendix A.4). The comparison is summarized in Table 4.4. The predicted plateau composition

agrees with the equilibrium values to within approximately 0.2 percentage points for all species, confirming that the reduced mechanism relaxes to the correct thermodynamic equilibrium within the furnace.

Table 4.4: CFD-predicted bulk composition in the plasma case compared against the equilibrium composition of dissociated CO_2 at the corresponding bulk temperature (~2898 °C, 1 atm), computed by Gibbs free energy minimization (Appendix A.4).

	CO_2 [%]	CO [%]	O_2 [%]	O [%]
CFD (plateau)	30.8	43.5	17.6	8.2
Equilibrium (2898 °C)	30.6	43.5	17.6	8.3

The radial species distributions follow the same near-uniform structure as the radial temperature profiles, with a centerline feature above an otherwise uniform background; for CO_2 this feature is inverted, with a centerline dip reflecting its depletion in the dissociated core. They are therefore not shown.

4.4 Comparison of Hydrogen and Plasma Cases

The hydrogen and plasma cases were both run at a 40 kW load with adiabatic walls, allowing the two heating approaches to be compared directly. Neither case has experimental validation data, so the comparison characterizes the model behavior rather than providing validated quantitative predictions. Table 4.5 summarizes the key differences.

The most notable distinction is in the radial thermal field. The hydrogen case produces localized hot reaction zones bounded by cold unreacted air, whereas the plasma case distributes heat nearly uniformly across the cross-section. This greater uniformity may be advantageous in heating applications where an even thermal field is desirable. The substantially higher outlet temperature of the plasma case is a consequence of its lower total mass flow rate at the same thermal load, rather than a difference in heating efficiency.

Table 4.5: Summary comparison of the hydrogen combustion and CO_2 plasma heating cases, both at 40 kW with adiabatic walls.

	Hydrogen combustion	CO_2 plasma heating
Where heat enters	Inside the furnace (flame)	Upstream in the heater
Peak temperature	2230 °C at the flame	3020 °C at the inlet
Outlet temperature	1800 °C	2900 °C
Total mass flow rate	$13.4\,g\,s^{-1}$	$4.91\,g\,s^{-1}$
Radial field	Swirl double-peak → single core	Narrow peak on uniform background
Chemistry	Burns to completion (H_2O)	CO_2 dissociates, partly recombines

5

Conclusion

This thesis developed and validated a CFD model of propane combustion in the Chalmers 100 kW unit, and adapted it to model hydrogen combustion and CO_2 plasma heating, in order to characterize and compare the thermal and chemical behavior of the three configurations.

The propane model reproduced the experimental data with reasonable accuracy once the flame had stabilized. From port M3 onward, the eddy-dissipation concept predictions captured the bulk centerline and radial temperature and major species profiles, and the area-weighted outlet composition agreed with the stoichiometric expectation for all three propane model combinations, confirming that the global mass balance was preserved. The principal deficiency was that the flame did not anchor at the burner but stabilized further downstream, so the near-burner region at M2 was not captured. The cause of this lift-off could not be isolated from the steady-state results; the reaction mechanism, uncertainty in the as-built swirl, and the steady quarter-domain treatment of the precessing vortex core are all plausible contributors. Comparing the reaction mechanisms, the Jones-Lindstedt mechanism produced sharper and more physically representative radial gradients than the Westbrook-Dryer mechanism, but exhibited more pronounced lift-off. On balance, the propane case established a modeling framework, namely the realizable $k - \varepsilon$ model, the eddy-dissipation concept, and the discrete ordinates method coupled with a weighted-sum-of-gray-gases model on a quarter domain, that was judged sufficient to carry forward to the hydrogen and plasma cases.

The hydrogen and plasma cases, for which no experimental data were available, revealed distinct thermal and chemical behavior. The hydrogen flame anchored immediately at the burner with no lift-off, reaching a centerline peak of approximately 2230 °C, likely an over-prediction owing to the single-step mechanism. The plasma case behaved fundamentally differently: the energy was deposited upstream of the furnace, so the gas entered already at its maximum temperature of approximately 3020 °C and cooled through the domain, with CO_2 dissociating in the heater and partially recombining as the gas cooled. At the same 40 kW load, the plasma case maintained a substantially higher and more radially uniform outlet temperature than the hydrogen case, owing to its smaller thermal mass and the absence of the swirl-driven reaction structure present in the combustion cases. This greater thermal uniformity may be advantageous in heating applications where a uniform thermal field is desirable, whereas the localized hot reaction zones of the combustion cases produce a less even distribution.

Overall, the work demonstrates that a CFD framework validated on propane combustion can be adapted to provide a first characterization of hydrogen and CO_2 plasma heating in the same unit, giving an indication of how a transition away from fossil combustion would alter the thermal field. The hydrogen and plasma results should be regarded as model characterizations rather than validated predictions, pending experimental data from the modified unit.

5.1 Future Work

Several avenues would strengthen and extend this work. A full three-dimensional transient simulation would allow the precessing vortex core to be represented and its contribution to the propane flame anchoring to be assessed, which the steady quarter-domain model could not isolate. Including radical reaction steps in the global reaction mechanisms is also a promising alternative to examine the anchoring issue. For the hydrogen case, a reduced or detailed kinetic mechanism would better capture the peak flame temperature than the single-step mechanism used here. For the plasma case, the dependence of the outlet composition on the cooling rate could be explored; a more rapid cooling might retain more of the dissociated CO, while slower cooling promotes recombination towards CO_2, and which is preferable would depend on the intended use of the product gas. The analysis could also be extended to decompose the radiative and convective heat transfer contributions across the configurations, and to examine velocity fields and residence times, which are relevant to the broader question motivating this study: how fossil-fuel heating might be replaced by hydrogen or plasma in high-temperature industrial processes. Finally, experimental data from the modified unit, once operational, would enable validation of the hydrogen and plasma models, which currently rely on the propane case as their only validated baseline.

Bibliography

[1] Government of Sweden. *Sweden's Climate Policy Framework*. https://www.government.se/articles/2021/03/swedens-climate-policy-framework/. Accessed: 24 February 2026. 2021.

[2] B. Andersson, R. Andersson, L. Håkansson, M. Mortensen, R. Sudiyo, and B. van Wachem. *Computational Fluid Dynamics for Engineers*. 14th ed. Cambridge University Press, 2018.

[3] T.-H. Shih, W. W. Liou, A. Shabbir, Z. Yang, and J. Zhu. "A new k-ε eddy viscosity model for high Reynolds number turbulent flows". In: *Computers & Fluids* 24.3 (1995), pp. 227–238.

[4] F. R. Menter. "Two-equation eddy-viscosity turbulence models for engineering applications". In: *AIAA Journal* 32.8 (1994), pp. 1598–1605.

[5] K. W. Ragland and K. M. Bryden. *Combustion Engineering*. 2nd ed. CRC Press, 2011.

[6] A. K. Gupta, D. G. Lilley, and N. Syred. *Swirl Flows*. Abacus Press, 1984.

[7] ANSYS, Inc. *Ansys Fluent Theory Guide*. Release 2025 R2. Ansys, Inc. Canonsburg, PA, 2025.

[8] B. F. Magnussen and B. H. Hjertager. "On mathematical modeling of turbulent combustion with special emphasis on soot formation and combustion". In: *Symposium (International) on Combustion* 16.1 (1977), pp. 719–729.

[9] B. F. Magnussen. "On the structure of turbulence and a generalized eddy dissipation concept for chemical reaction in turbulent flow". In: *19th AIAA Aerospace Sciences Meeting*. January 12–15. St. Louis, Missouri, 1981.

[10] W. P. Jones and R. P. Lindstedt. "Global reaction schemes for hydrocarbon combustion". In: *Combustion and Flame* 73.3 (1988), pp. 233–249.

[11] M. F. Modest. *Radiative Heat Transfer*. 3rd ed. Academic Press, 2013.

[12] S. Hjärtstam. "Radiative Properties and Combustion Chemistry in Oxy-Fuel Flames – Experiments and Modelling Elements". PhD thesis. Chalmers University of Technology, 2011.

[13] The Engineering Toolbox. *Heating values of Fuel Gases*. https://www.engineeringtoolbox.com/heating-values-fuel-gases-d_823.html. Accessed: March 2026. 2005.

[14] W. Wang, Y. Cao, and T. Okaze. “Comparison of hexahedral, tetrahedral and polyhedral cells for reproducing the wind field around an isolated building by LES”. In: *Building and Environment* 195 (2021), p. 107717. DOI: 10.1016/j.buildenv.2021.107717.

[15] T. F. Smith, Z. F. Shen, and J. N. Friedman. “Evaluation of Coefficients for the Weighted Sum of Gray Gases Model”. In: *Journal of Heat Transfer* 104.4 (1982), pp. 602–608.

[16] K. Andersson and F. Johnsson. “Flame and radiation characteristics of gas-fired O2/CO2 combustion”. In: *Fuel* 86.5-6 (2007), pp. 656–668.

[17] E. Ehlmé, A. Gunnarsson, F. Normann, and K. Andersson. “Updated Weighted-Sum-of-Gray-Gases Model Parameters for a Wide Range of Water and Carbon Dioxide Concentrations and Temperatures up to 5000 K”. In: *ACS Omega* 10.3 (2025), pp. 2978–2985. DOI: 10.1021/acsomega.4c09432.

[18] D. G. Goodwin, H. K. Moffat, I. Schoegl, R. L. Speth, and B. W. Weber. *Cantera: An Object-oriented Software Toolkit for Chemical Kinetics, Thermodynamics, and Transport Processes*. https://www.cantera.org. Version 3.2.0. 2025. DOI: 10.5281/zenodo.17620923.

[19] G. P. Smith, D. M. Golden, M. Frenklach, N. W. Moriarty, B. Eiteneer, M. Goldenberg, C. T. Bowman, R. K. Hanson, S. Song, W. C. Gardiner Jr., V. V. Lissianski, and Z. Qin. *GRI-Mech 3.0*. http://combustion.berkeley.edu/gri-mech/.

A

Appendix 1

This appendix contains the full experimental measurement data used for validation and supplementary radial profiles not included in the main text.

A.1 Experimental Measurement Data

Temperature [C]										
Radial pos. [mm]	-400	-300	-200	-100	-50	0	50	150	250	350
Port M2	698.4	735.7	795.6	1073.0	1731.7	1545.0	1734.5	-	-	-
Port M3	711.6	770.3	833.5	1147.8	1654.2	1582.0	1619.9	1045.8	900.7	743.5
Port M4	776.4	839.2	920.8	1266.5	1529.4	1553.9	1512.0	1236.2	1025.8	939.8
Port M5	869.1	909.5	1041.7	1229.2	1301.1	1341.1	1354.6	1240.6	1026.0	866.7

Table A.1: Measurements of temperature from ports M2-M5 at different radial position.

	Species composition													
	Radial pos. [mm]	-400	-300	-200	-150	-100	-50	0	25	50	100	150	250	350
	Port M2	2.95	2.99	3.23	-	13.57	1.13	0.08	-	0.08	5.63	-	-	-
	Port M3	3.08	3.12	4.42	6.67	7.95	0.20	0.04	-	0.07	1.60	-	-	-
O_2 [%dry]	Port M4	3.10	3.29	4.58	5.53	3.53	0.42	0.24	-	0.28	0.62	-	-	-
	Port M5	3.18	3.13	3.34	3.20	2.56	1.68	1.16	-	0.93	0.97	-	-	-
	Port M6	-	-	-	-	-	-	3.21	3.13	3.09	2.95	2.95	2.90	2.88
	Port M2	0.01	0.01	0.00	-	0.18	2.15	10.30	-	10.21	0.15	-	-	-
	Port M3	0.01	0.01	0.01	0.01	0.06	4.18	7.15	-	6.32	0.92	-	-	-
CO [%dry]	Port M4	0.01	0.01	0.01	0.03	0.38	2.04	2.74	-	2.82	1.50	-	-	-
	Port M5	0.00	0.00	0.01	0.02	0.07	0.16	0.31	-	0.44	0.42	-	-	-
	Port M6	-	-	-	-	-	-	0.011	0.003	0.005	0.002	0.002	0.008	0.000
	Port M2	11.46	11.46	11.38	-	4.97	11.16	6.99	7.09	9.71	-	-	-	-
	Port M3	10.59	11.38	10.59	9.03	8.20	10.62	8.97	9.51	11.86	-	-	-	-
CO_2 [%dry]	Port M4	11.36	11.30	10.50	9.93	10.89	11.86	11.56	11.51	12.14	-	-	-	-
	Port M5	10.18	11.40	11.28	11.31	11.66	12.22	12.47	12.55	12.57	-	-	-	-
	Port M6	-	-	-	-	-	-	10.12	10.26	10.31	10.14	10.17	10.14	9.86
	Port M2	10.10	12.74	17.21	-	8.83	11.28	13.19	14.52	15.59	-	-	-	-
	Port M3	8.25	13.23	13.07	11.57	10.53	10.39	14.00	15.01	15.64	-	-	-	-
H_2O [%]	Port M4	6.97	13.18	13.12	12.21	11.85	9.66	14.94	17.66	15.13	-	-	-	-
	Port M5	16.27	13.64	13.58	13.36	12.70	11.76	14.18	13.72	15.22	-	-	-	-
	Port M6	-	-	-	-	-	-	16.25	16.49	16.46	16.25	16.27	16.27	15.77

Table A.2: Measured gas composition from ports M2–M6 at different radial positions.

A.2 Figures

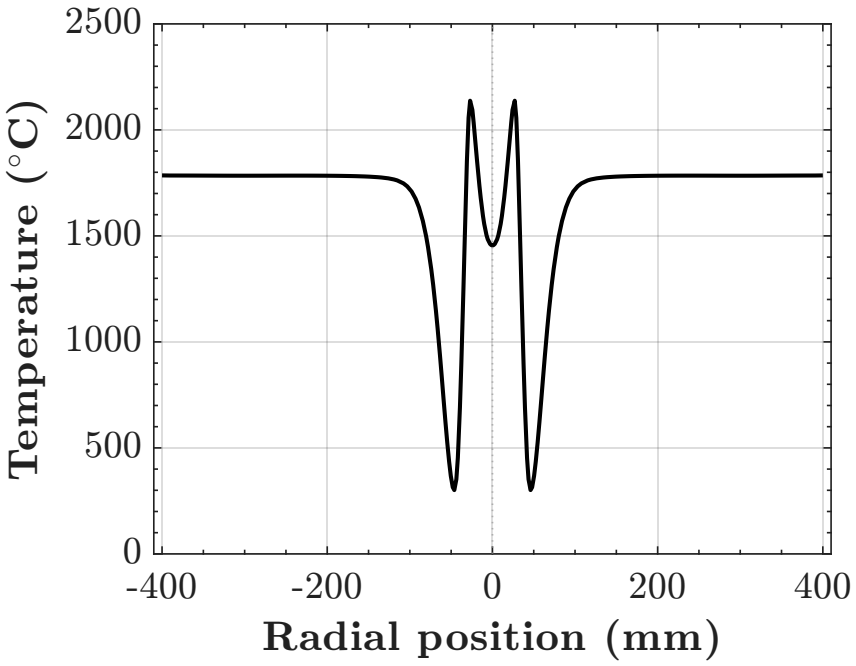

Figure A.1: Radial temperature profile at M2 predicted from EDC using 1-step mechanism for H_2-combustion.

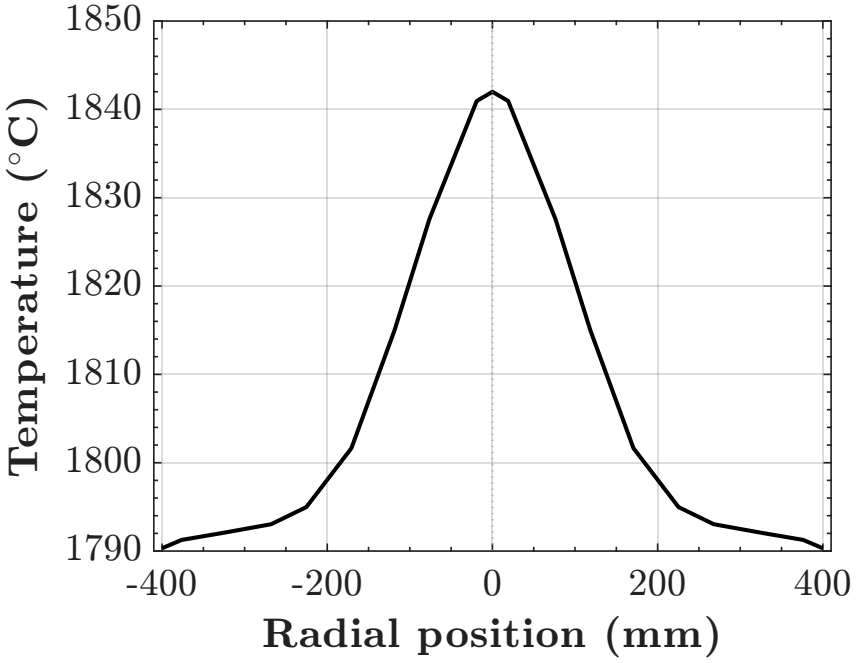

Figure A.2: Radial temperature profile at M7 predicted from EDC using 1-step mechanism for H_2-combustion.

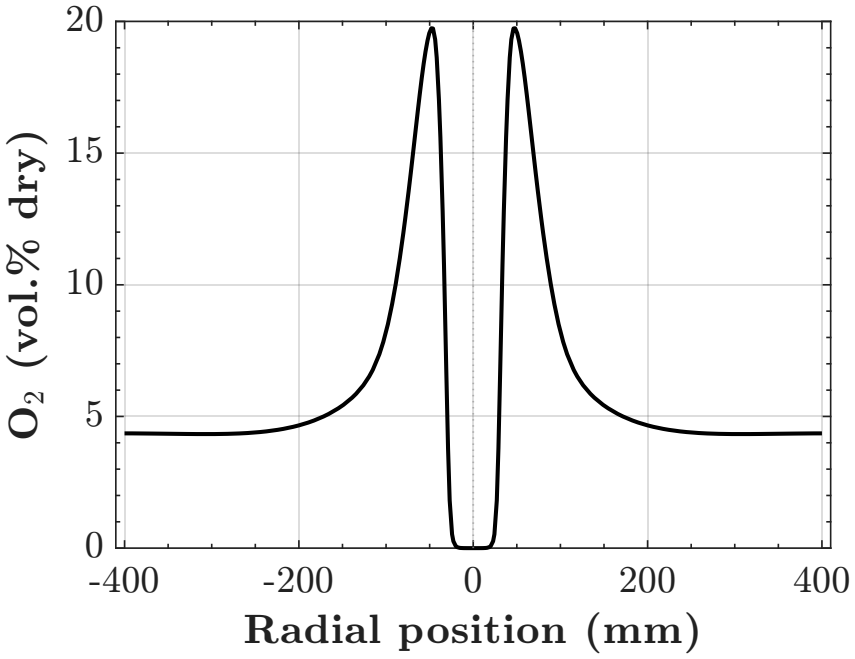

Figure A.3: Radial O_2 profile at M2 predicted from EDC using 1-step mechanism for H_2-combustion.

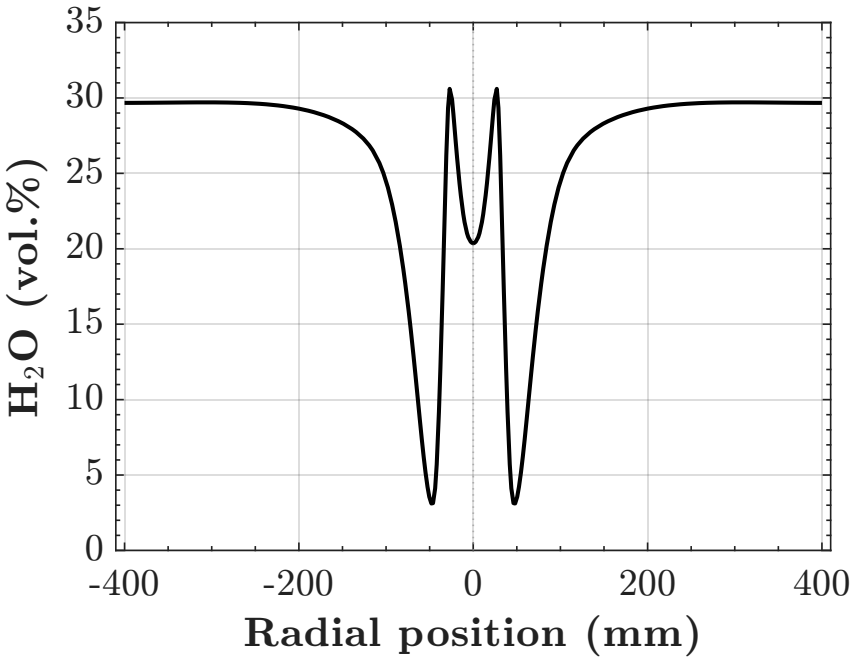

Figure A.4: Radial H_2O profile at M2 predicted from EDC using 1-step mechanism for H_2-combustion.

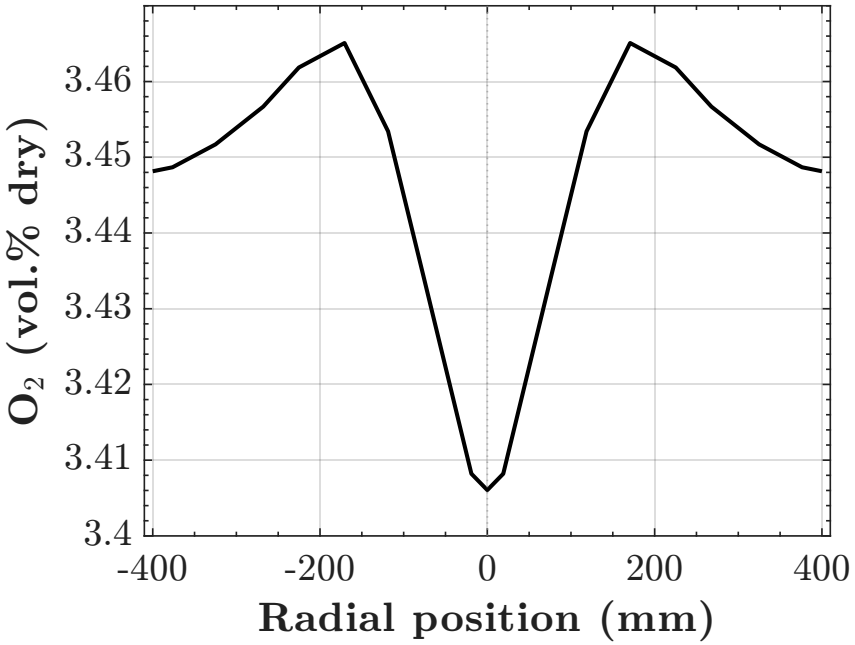

Figure A.5: Radial O_2 profile at M7 predicted from EDC using 1-step mechanism for H_2-combustion.

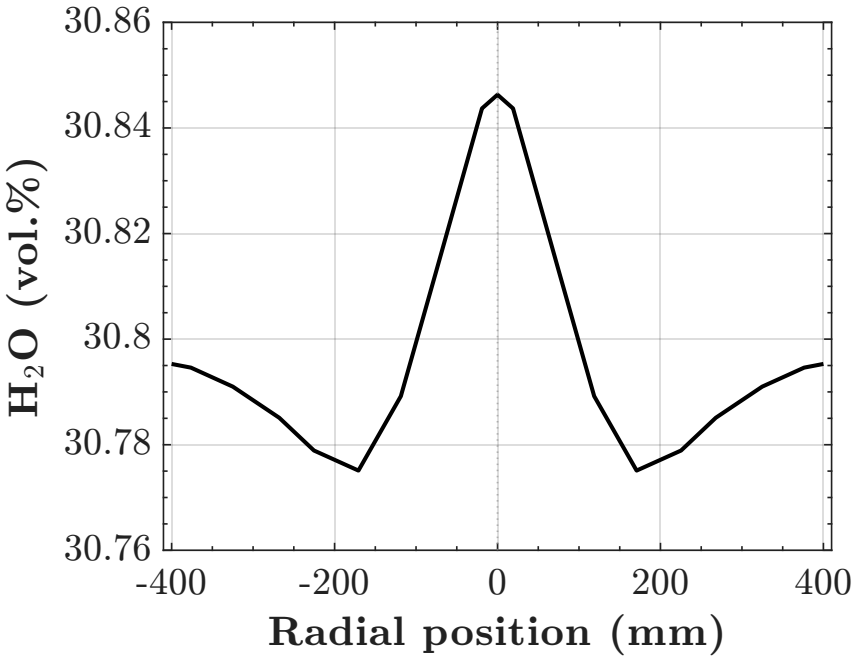

Figure A.6: Radial H_2O profile at M7 predicted from EDC using 1-step mechanism for H_2-combustion.

A.3 Reactions

Table A.3: Reduced reaction mechanism for CO_2 dissociation and recombination used in the plasma case, $k = AT^{\beta}\exp(-E_a/RT)$.

	Reaction	A	β	E_a
R1	$2\,O \rightleftharpoons O_2$	1.20×10^{17}	-1.0	0
R2	$O + CO \rightleftharpoons CO_2$	1.80×10^{10}	0	2385
R3	$O_2 + CO \rightleftharpoons O + CO_2$	2.50×10^{12}	0	47 800
R4	$C + O_2 \rightleftharpoons O + CO$	5.80×10^{13}	0	576

Units consistent with mol, cm, s, K; E_a in cal/mol. Third-body and pressure-dependence terms in the source CHEMKIN mechanism are retained in the simulation but omitted from this table for clarity.

A.4 Equilibrium Composition of Dissociated CO_2

This appendix section documents the equilibrium calculation referenced in Section 3.8. The chemical equilibrium composition of CO_2 gas was computed at fixed temperature and atmospheric pressure by Gibbs free energy minimization, using the open source software Cantera, version 3.2.0 [18], with thermodynamic data (NASA polynomial fits) from GRI-Mech-3.0 [19]. The GRI-Mech 3.0 thermodynamic data are valid to approximately 3500 K, which covers the furnace temperatures where the comparison is made. Due to the source region being outside of the GRI-Mech 3.0 validity range, this comparison is not extended to this region. The resulting composition is given in Table A.4 and the Python script used is provided in Listing A.1.

Table A.4: Equilibrium mole fractions of dissociated CO_2 at 1 atm, computed by Gibbs free energy minimization. Atomic carbon is below 10^{-5} % at all temperatures shown and is omitted.

T [°C]	CO_2 [%]	CO [%]	O_2 [%]	O [%]
2700	45.6	34.9	15.4	4.0
2800	37.7	39.5	16.8	5.9
2898	30.6	43.5	17.6	8.3
3000	24.0	46.9	17.8	11.3
3020	22.9	47.5	17.8	11.9
3100	18.6	49.4	17.3	14.7

The furnace inlet state (~3020°C) is under-dissociated in the CFD prediction. The equilibrium of CO_2 at the furnace inlet is approximately 23%, substantially below the predicted inlet value of approximately 35% (Figure 4.15c). The gas thus leaves the heater chemically lagging behind its temperature, and the continued dissociation over the first ~100-200 mm represents the chemistry relaxing towards equilib-

rium. This observation is consistent with the endothermic temperature dip in Figure 4.13.

Listing A.1: Cantera script used to compute the equilibrium compositions in Table A.4.

```
import cantera as ct

P = ct.one_atm
SPECIES = ["CO2", "CO", "O2", "O", "C"]
TEMPERATURES_C = [2700, 2800, 2898, 3000, 3020, 3100]

gas = ct.Solution("gri30.yaml")

for T_C in TEMPERATURES_C:
    gas.TPX = T_C + 273.15, P, {"CO2": 1.0}
    gas.equilibrate("TP")  # Gibbs minimization at constant T, P
    x = [gas.X[gas.species_index(s)] * 100 for s in SPECIES]
    print(T_C, [f"{v:.3f}" for v in x])
```

DEPARTMENT OF ENVIRONMENTAL AND ENERGY SCIENCES
CHALMERS UNIVERSITY OF TECHNOLOGY
Gothenburg, Sweden
www.chalmers.se

CHALMERS
UNIVERSITY OF TECHNOLOGY